Research Square

Preprints are preliminary reports that have not undergone peer review.
They should not be considered conclusive, used to inform clinical practice,
or referenced by the media as validated information.

Post-Earthquake Dust Contamination: Elemental Composition, Asbestos, and Inorganic Fibers in a GIS-Based Environmental Health Assessment of Hatay, Türkiye

Kadir Ulutaş

kulutas@purdue.edu

Istanbul Medeniyet University

Enes Özkök

Karabük University

Emre Yücer

Karabük University, TOBB Vocational School of Technical Sciences

Dilara Potur

Istanbul Medeniyet University

Abdulkadir Keskin

Istanbul Medeniyet University

Halis Simsek

Purdue University

Pınar Ergenekon

Gebze Technical University

Mehmet Salim Öncel

Gebze Technical University

Research Article

Keywords: Disaster management, Natural hazards, Public Health, Aerosols and particles, Pollution: urban and regional/global

Posted Date: October 26th, 2026

DOI: https://doi.org/10.21203/rs.3.rs-11245758/v1

License: This work is licensed under a Creative Commons Attribution 4.0 International License.
Read Full License

Additional Declarations: No competing interests reported.

Post-Earthquake Dust Contamination: Elemental Composition, Asbestos, and Inorganic Fibers in a GIS-Based Environmental Health Assessment of Hatay, Türkiye

Kadir Ulutaş[1,2*], Enes Özkök[3], Emre Yücer[4], Dilara Potur[1], Abdulkadir Keskin[5], Halis Simsek[2], Pınar Ergenekon[6], Mehmet Salim Öncel[6]

[1] Istanbul Medeniyet University, Faculty of Health Sciences, Department of Health Management, Istanbul, Türkiye

[2] Purdue University, College of Engineering, Department of Agricultural and Biological Engineering, West Lafayette, IN, USA

[3] Karabük University, Faculty of Engineering, Department of Environmental Engineering, Karabük, Türkiye

[4] Karabük University, TOBB Vocational School of Technical Sciences, Karabük, Türkiye

[5] Istanbul Medeniyet University, Faculty of Engineering and Natural Sciences, Department of Statistics, Istanbul, Türkiye

[6] Gebze Technical University, Faculty of Engineering, Department of Environmental Engineering, Kocaeli, Türkiye

[*]Corresponding author: Kadir Ulutaş kulutas@purdue.edu; kadir.ulutas@medeniyet.edu.tr

Abstract: The twin earthquakes that struck Kahramanmaraş, Türkiye on February 6, 2023, caused widespread destruction and loss of life. This study offers a unique perspective on multi-pollutant assessment in post-earthquake urban areas by detecting heavy metals, asbestos, and inorganic fibers in dust samples taken from collapsed building foundations in the Hatay city center, and identifying potentially sensitive areas in terms of environmental and public health using GIS. Dust samples collected from 61 locations were sieved into three size fractions, and elemental analyzed via XRF. Qualitative pollution was assessed using the enrichment factor and ecological risk index, and spatial distribution maps generated for heavy metal concentration. SEM-EDS identified 1,370 fibrous objects across 23 sites, including 10 potentially asbestos fibers. Despite the extremely small absolute number of confirmed asbestos fibers, asbestos was detected primarily at sites consisting of older informal housing, suggesting legacy contamination. Spatial analysis showed elemental concentrations positively correlated with demolished building age and proximity to traffic arteries, revealing distinct anthropogenic contamination hotspots. The ecological risk index of 168.6 indicated moderate ecological risk for the overall study area. High concentrations of major elements such as Ca, Si, Mg, Fe, and Al are consistent with composition of construction and demolition wastes, particularly those related to cement and raw materials, and were analyzed using PCA in this study. These findings highlight the need for protective measures against dust inhalation in post-earthquake areas and underscore the importance of further research on airborne exposure for environmental and public health.

Keywords: Disaster management, Natural hazards, Public Health, Aerosols and particles, Pollution: urban and regional/global

Highlights

1,370 fibrous objects were identified; 10 were confirmed as asbestos.

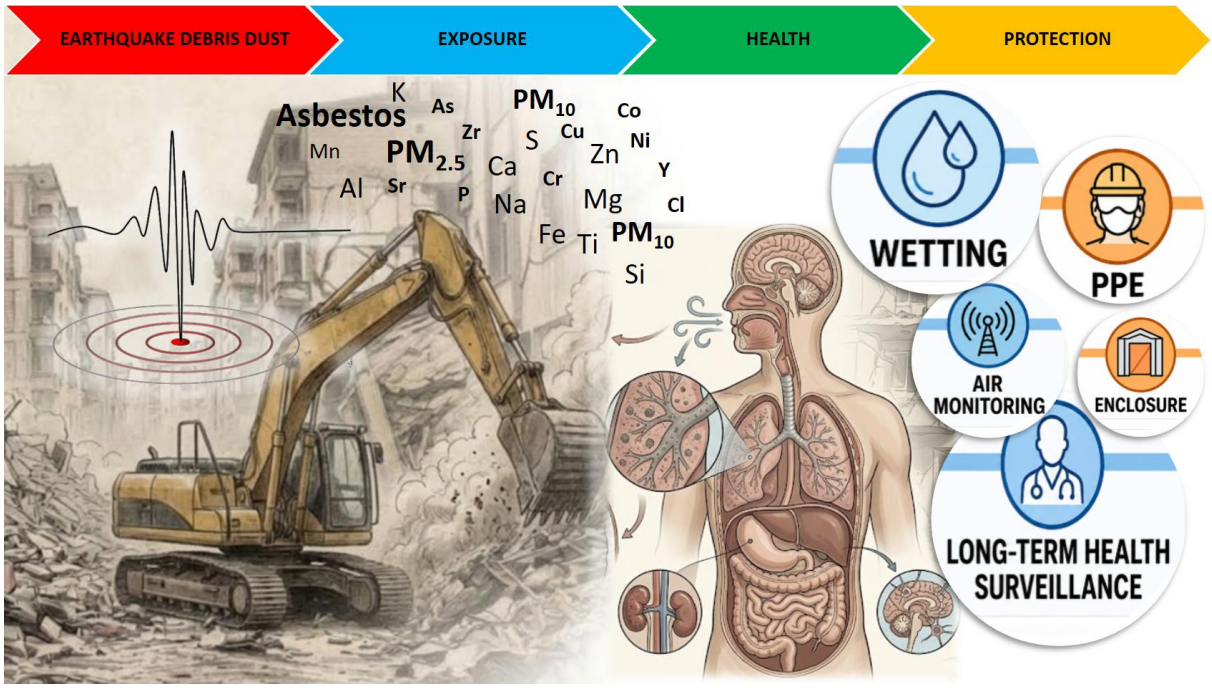
Ca, Si, Mg, Fe, and Al indicated construction waste.

Ni, S, and Ca showed very high enrichment.

As and Ni showed high ecological risk.

PCA linked elements to cement and raw materials.

Graphical abstract


EARTHQUAKE DEBRIS DUST
EXPOSURE
HEALTH
PROTECTION
Asbestos
K
As
Mn
PM2.5
Zr
S
Cu
PM10
Co
Ni
Zn
Y
Al
Sr
P
Ca
Cr
Na
Mg
Cl
Fe
Ti
PM10
Si
WETTING
PPE
AIR MONITORING
ENCLOSURE
LONG-TERM HEALTH SURVEILLANCE

1. Introduction

On February 6, 2023, two major earthquakes centered in Kahramanmaraş, Türkiye, caused widespread structural destruction and substantial loss of life across 10 provinces. The seismic sequence, associated with rupture of the East Anatolian Fault, began with a magnitude 7.7 earthquake at 4:17 a.m. local time, followed approximately nine hours later by a magnitude 7.6 earthquake at 1:24 p.m., further intensifying the damage (Maden, 2023). Damage assessments indicated that, among approximately 1.52 million buildings inspected, more than 202,000 had collapsed, sustained severe damage, or required urgent demolition (ÇBS, 2023). The unprecedented scale of destruction was estimated to generate more than 170 million tons of earthquake-related debris across the affected provinces (DHA, 2023). Hatay Province was among the most severely affected areas, with reports documenting 13,517 collapsed buildings, 8,162 requiring urgent demolition, and 67,346 classified as heavily damaged based on completed or contested damage assessments (AA, 2023).

Beyond the immediate physical devastation, large-scale disasters such as earthquakes can generate secondary environmental hazards, particularly particulate matter (PM) released during building collapses and subsequent debris removal activities. Exposure to these airborne particles through inhalation can pose significant risks to human health, while their deposition can adversely affect air, water, soil, and vegetation. The potential health effects of particulate matter depend largely on particle size, size distribution, chemical composition, and route of exposure (Liu et al., 2014; Briffa et al., 2020). The impacts of building demolition on air quality have been investigated in several studies, commonly through particulate matter sampling using dust collection plates positioned near demolition sites and high-volume air samplers (Jacobs et al., 2013; Ding et al., 2016). Such studies provide valuable information on the generation, transport, and characteristics of demolition-related particulate matter and can support authorities in developing strategies to minimize environmental and public health impacts associated with demolition and debris management (Ding et al., 2016).

Among the constituents of particulate matter, heavy metals, such as lead, cadmium, and zinc, are of particular concern due to their persistence in the environment and living tissue (Kanwar et al. 2020). This characteristic makes street dust a valuable indicator for assessing environmental contamination (Delibašić et al. 2020), and it has been widely utilized as an environmental medium in numerous studies evaluating heavy metal pollution levels in urban areas (Kafle et al. 2022; Kravkaz Kuşçu et al. 2022; Marjovvi et al. 2022; Moskovchenko et al. 2022; Ulutaş 2023a; Abujayyab et al. 2025).

Earthquake-generated dust can also contain hazardous materials, including asbestos and other inorganic fibers, substantially degrading air quality and posing serious risks to public health (Oral et al., 2025). These fine, rigid fibers can readily become airborne and, following exposure, penetrate the human body and become lodged in the respiratory and gastrointestinal systems (Güney and Yılmaz, 2023; Dimiskovska, 2010; Metin et al., 2023). Because the body has limited ability to break down or eliminate retained asbestos fibers, exposure can result in long-term health effects and diseases that may not become apparent until many years later (Dimiskovska, 2010; Metin et al., 2023). Asbestos minerals are broadly classified into serpentine (chrysotile) and amphibole (crocidolite, amosite, anthophyllite, actinolite, and tremolite) groups, and all forms of asbestos are classified as carcinogenic by major international health organizations (IARC, 2012). Although the use of asbestos was banned in Türkiye in 2010, it had previously been widely used as an insulation and construction material, particularly from

the 1980s through the early 2000s. Consequently, the collapse and demolition of older buildings can release asbestos-containing materials into the surrounding environment, creating potential exposure risks for nearby residents, demolition workers, and their families (Tokkamiş and Uraz, 2022).

In Hatay, it had been observed that dust from demolition and debris removal became a major source of air pollution. Based on the critical need for assessing contamination risks in post-earthquake areas and considering relevant literature and regulations, the objective of this study was to comprehensively examine the dust accumulated on the foundations of collapsed buildings in Hatay by analyzing its heavy metal, asbestos, and other inorganic fiber content, and to identify sensitive areas for public health management with GIS, thereby contributing to the existing literature on disaster-related environmental contamination. The dust on building foundations was sampled as it represents a composite accumulation of all dust deposited in the earthquake's immediate aftermath and subsequent debris removal, similar to methods used in street dust (Ulutaş 2022; 2023b). To achieve this objective, a total of 61 dust samples were collected from various points across the affected area in Hatay. All 61 samples were analyzed for major and minor element content using Wavelength Dispersive X-ray Fluorescence (XRF). Additionally, a subset of 23 dust samples underwent analysis using Scanning Electron Microscopy (SEM) coupled with Energy-Dispersive X-ray Spectroscopy (EDS) to identify inorganic fibrous structures and asbestos. Pollution levels were determined using Enrichment Factor (EF) and Ecological Risk Index (ERI) calculations. Spatial distribution maps of the analyzed parameters were created using GIS to identify areas potentially sensitive in terms of environmental and public health across the city.

2. Materials and Methods

2.1. Information on Study Area and Sampling Locations

Hatay, one of the provinces most severely affected by the February 6 Kahramanmaraş earthquakes, was selected as the study area due to the extensive structural damage sustained across the region. The scale of the destruction necessitated widespread demolition and debris removal operations involving both manual and machine-assisted methods. These activities, combined with the handling, transportation, and disposal of large quantities of demolition debris, resulted in substantial dust generation and the potential release of particulate matter into the surrounding environment.

In the immediate aftermath of the disaster, emergency responders focused on critical priorities such as debris removal, providing shelter and food, healthcare, and epidemic control. The large scale and urgency of the demolition process meant that waste materials in buildings, such as construction materials and household items, were not sorted before demolition. This practice generated mixed debris. Furthermore, the high risks involved made the separation of hazardous waste impractical, and conventional dust suppression methods were also not implemented. These conditions led to the wide dispersion of airborne dust from demolished structures into the environment during demolition and debris removal operations, with subsequent uncontrolled deposition.

As a result, post-demolition, dust naturally accumulated on the exposed surfaces of building foundations. This accumulated dust represents a composite sample reflecting the mixed materials present in the collapsed structures that settled from the air. Collecting samples from these foundation surfaces allowed for an assessment of the composition of this earthquake-related dust and the identification of key pollutants present. In the study area, due

to the magnitude of the earthquake and the damage to tens of thousands of buildings, the available resources only allowed for the collection of composite samples.

In this study, a total of 61 dust samples were collected from the surface of collapsed building foundations in the city of Hatay between April 28 and May 13, 2023, after initial debris removal and demolition work had been completed. Sampling locations were strategically selected from areas that experienced the highest rates of demolition to ensure representative coverage across the most impacted parts of the city (Figure 1). Each sample, weighing between 1.0 and 1.5 kg, was collected from an approximate area of 1.0–1.5 m² on the foundation surface using clean plastic brooms and dustpans. The collected samples were then placed into sealed plastic bags, labeled with unique identifiers, and stored in a cool, dry environment to preserve them before analysis.

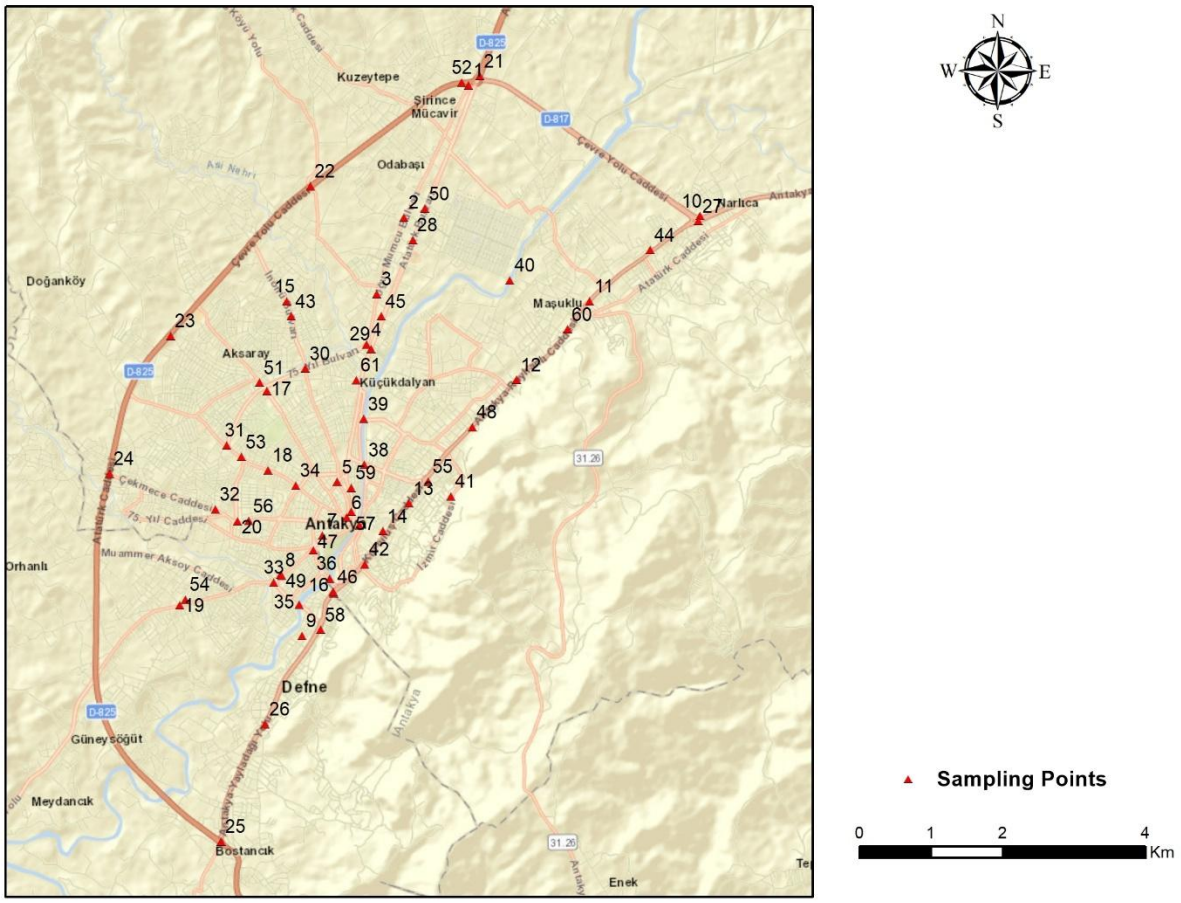


Fig. 1 Sampling Points in the Study Area.

2.1. Sample Preparation and Content Analysis

Upon arrival at the laboratory, the collected dust samples were oven-dried at 105 °C to remove moisture. The dried samples were then sieved and separated into three particle-size fractions as follows: (i) <38 µm, (ii) 38 µm–2 mm, and (iii) >2 mm. The mass of each fraction was measured, and its percentage contribution to the total sample mass was calculated.

Following sieve analysis, the elemental composition of the different dust fractions was determined using a wavelength-dispersive X-ray fluorescence (XRF) spectrometer (Rigaku Primus IV). For XRF analysis, 3 grams of each specimen were prepared by pelletizing under 40 tons of pressure to ensure uniformity. The SQX (Semi-Quantitative X-ray) analysis mode, integrated into the instrument, was selected for measurements. This eliminates the need for any pre-calibration and allows for the determination of approximate sample concentrations. The SQX analysis method operates on the basis of X-ray interaction models and pre-defined fundamental parameters (basic physical constants). Fluxana validation RAW V01 and V06 OXIDE-FB-PAK (Rigaku) are used for this purpose. This allows semi-quantitative calculations of the mass percentages of oxides and elements in the sample without the need for calibration standards. This method has been shown to be an ideal analytical tool to determine the chemical composition of samples with highly satisfactory accuracy (Smoliński et al. 2022), as it offers a rapid and a cost-effective solution for studies involving large numbers of samples (González & Saadatkhah, 2024). Both the sieve and elemental analyses were performed at the Gebze Technical University, Institute of Earth and Marine Sciences Laboratory in Turkiye. The results obtained from the elemental analysis were statistically evaluated using IBM SPSS Statistics software.

2.2. Assessment of Pollution Levels Using Enrichment Factor and Ecological Risk Index

To evaluate the enrichment degree of specific elements in debris dust relative to background soil composition, the Enrichment Factor (EF) was calculated as defined by Mason (1966) (Equation 1):

$$\mathrm{EF} = \frac{\left(C_x/C_{Al}\right)_{sample}}{\left(C_x/C_{Al}\right)_{ref.}} \quad (1)$$

where $(C_x/C_{Al})_{sample}$ represents the concentration ratio of the element of interest (C_x) to iron (C_{Al}) in the dust sample, and $(C_x/C_{Al})_{ref.}$ represents the corresponding concentration ratio in the background soil sample. Al was selected as the reference element due to its abundance in the Earth's crust (Cesari et al. 2012; Mason, 1966). EF values were interpreted using the following categories: minimal (EF < 2), moderate (2 ≤ EF < 5), significant (5 ≤ EF < 20), high (20 ≤ EF < 40), and very high (EF ≥ 40).

To further investigate the pollution levels and assess the potential ecological risk posed by heavy metal contamination in the dust samples, the Ecological Risk Factor (ERF) and Ecological Risk Index (ERI) analyses were employed based on the methodology proposed by Hakanson (1980). The assessment began first by calculating the Contamination Factor ($\mathbf{C_f}$) for each toxic element (Equation 2):

$$Cf = \frac{C_i}{C_{i,n}} \quad (2)$$

where C_i represents the concentration of element i in the debris dust sample (mg/kg), and $C_{i,n}$ is its concentration in the Earth's crust.

The Ecological Risk Factor (ERF), which indicates potential health risks in an ecosystem, was calculated using Equation 3:

$$ERF = T_i \, X \, C_f \quad (3)$$

where C_f is the contamination factor, and T_i is the toxicological response factor proposed by Hakanson (1980) in his risk index approach. The ERF values were categorized as follows: low risk (ERF < 40), moderate risk (40 ≤ ERF < 80), moderate to high risk (80 ≤ ERF < 160), high risk (160 ≤ ERF < 320), and very high risk (ERF ≥ 320).

Finally, the Ecological Risk Index (ERI), representing the cumulative potential ecological risk from multiple elements, was calculated as the sum of the individual Ecological Risk Factors (Equation 4):

$$ERI = \sum_{i=1}^{n} ERF_i \quad (4)$$

Based on the calculated ERI values, the overall ecological risk was classified as follows: low ecological risk (ERI < 150), moderate ecological risk (150 ≤ ERI < 300), and significant ecological risk (300 ≤ ERI < 600) (Hakanson, 1980; Kara, 2020).

Although Enrichment Factor and Ecological Risk Index were not specifically developed for application in post-earthquake regions, they were used in this study to assess pollution levels.

2.3. Analysis of Fibrous Structures

A total of 23 dust samples with particle sizes smaller than 38 μm were selected to analyze fibrous structures. These samples were attached to 2.5 mm carbon adhesive tapes (Yang et al. 2020). For each sample, 50 distinct points were examined using a Quattro S Scanning Electron Microscope (Thermo Scientific, Waltham, MA, USA) located at Istanbul Medeniyet University's Center for Science and Advanced Technology. The Scanning Electron Microscopy (SEM) was operated at a magnification of 5000X, and each point was further analyzed using Energy-Dispersive X-ray Spectroscopy (EDS) to determine the elemental composition of any observed fibrous structures. This approach allowed for the assessment of both the morphology and chemical makeup of individual fibers (Stevulova et al. 2020).

The morphological features and dimensions (length and diameter) of each identified fiber were meticulously determined from the SEM images. In addition to these morphological characteristics, the fibrous structures' lengths, diameters, and chemical compositions were also analyzed. The classification of asbestos and other fibrous materials were based not only on dimensional parameters, but also on the compositional criteria associated with the six recognized types of asbestos (Table 1). Subsequently, the chemical composition obtained from EDS analysis was used to aid in the classification of asbestos and other fibrous structures. The classification of a fiber as asbestos was based on a combination of dimensional criteria and the presence of characteristic elements. Following the guidelines outlined in the *Occupational Health and Safety Implementation Guide for Asbestos Work* (AÇİSGUR, 2019), a fiber was considered asbestos if it exhibited a length greater than 5 μm, a diameter less than 3 μm, and a length-to-diameter ratio exceeding 3:1. In the SEM images, all fibrous and non-fibrous microscopic structures corresponding to this proportion were identified during the initial scanning. In addition to these dimensional thresholds, EDS analysis specifically focused on detecting the presence of silicon (Si) and magnesium (Mg), which

are key elemental indicators for asbestos. Fibers that did not contain detectable levels of these elements were presumed to be of organic origin. All SEM and EDS analyses were conducted in compliance with the applicable regulatory standards and best scientific practices to ensure the reliability and validity of the results.

Table 1. The asbestos types

Asbestos Type	Formula
Chrysotile (white asbestos)	$Mg_3[Si_2O_5](OH)_4$
Anthophyllite	$Mg_7[Si_8O_{22}](OH)_2$
Amosite (brown asbestos)	$Fe_7[Si_8O_{22}](OH)_2$
Crocidolite (blue asbestos)	$Na_2Fe_5[Si_8O_{22}](OH)_2$
Tremolite and Actinolite	$Ca_2(Mg, Fe^{2+})_5[Si_8O_{22}](OH)_2$

2.4. Preparation of Distribution Maps

This study employed Geographic Information System (GIS) tools to visualize heavy metal pollution levels and enrichment factor (ZF) values in dust samples collected from building foundations post-demolition and debris removal. Using the ArcMap module of the ArcGIS software, spatial distribution maps were generated based on the concentration levels of measured parameters. Sampling locations were georeferenced, and interpolated data were stored in a grid raster format. Additional geospatial datasets, including topographic maps and satellite imagery, were processed via GeoMedia and ArcGIS to create an updatable geodatabase. Given the limited number of sampling points, a geostatistical interpolation method, Inverse Distance Weighting (IDW), was applied to estimate pollution density across the study area (Wang and Liu, 2005; Nagalakshmi et al. 2016). The IDW method assigns values to unsampled locations based on the spatial relationship of measured points, assuming that closer points have a greater influence than distant ones. Consequently, the influence of a data point decreases with increasing distance, producing a smoothly modeled distribution surface (Li et al. 2017; Guo et al. 2021; Shafie et al. 2021; Xie et al. 2021). The relatively limited number of sampling points may lead to uncertainty and risk of over-interpretation in some spatial patterns. Therefore, map results should be considered a preliminary assessment, and interpretations should be made accordingly.

3. Results and Discussion

3.1. Results of Sieve Analyses

The results of the sieve analysis of the 61 samples collected from the study area are presented (Figure 2). The results indicated that particle sizes predominantly fell within the 38 µm–2 mm range for most samples, accounting for 41% to 90% (w/w) of the total sample mass. On average, the fraction smaller than 38 µm constituted 1.9% of the samples; the fraction between 38 µm–2 mm was 68.7%; and the fraction larger than 2 mm was 29.4%.

The fact that the majority of the dust is in the 38 µm to 2 mm range and above 2 mm suggests that a significant portion of the debris consists of coarser material from the collapsed buildings. Even though it represents a small percentage by weight, the <38 µm fraction is essential for evaluating inhalable particulate matter and its associated health risks, such as asbestos inhalation.

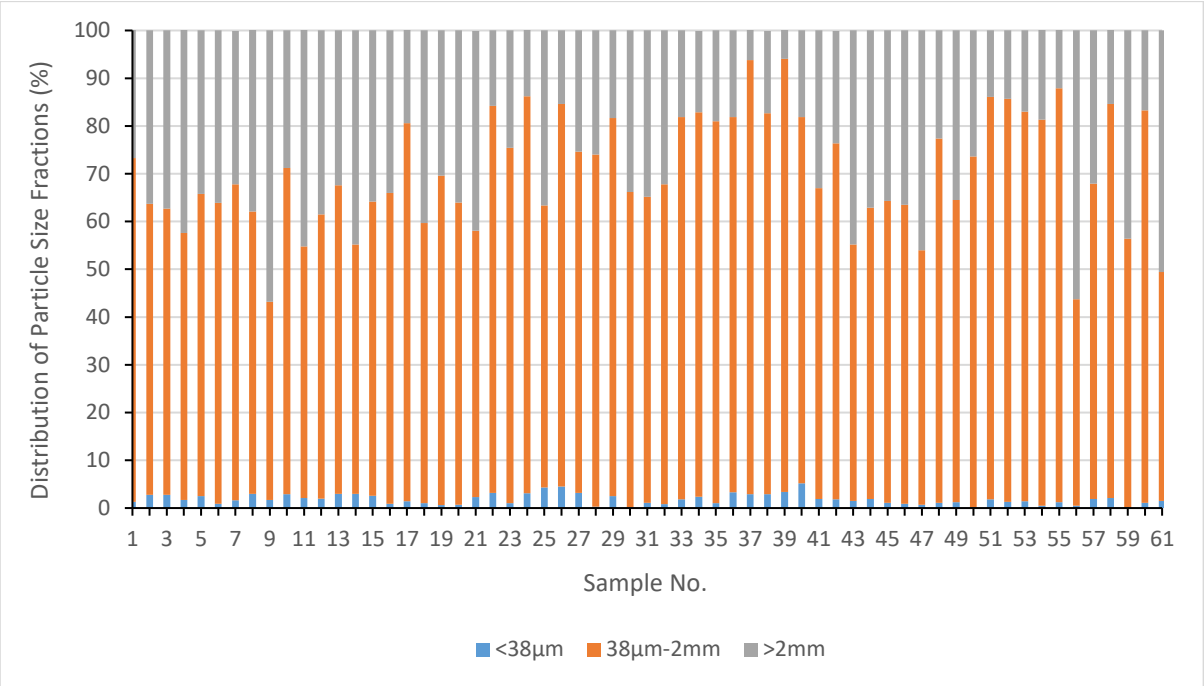


Fig. 2 Particle size distribution of 61 samples based on three size fraction classes (w/w).

3.2. Results of Major and Minor Elemental Analyses

Elemental analysis was conducted on all 61 post-demolition dust samples collected from building foundations in Hatay using a Wavelength Dispersive XRF device. The samples were analyzed to determine the concentrations of major and minor elements, presented as oxides (e.g., CaO, SiO_2, Fe_2O_3) and elemental concentrations (e.g., Ca, Si, Fe). A summary of the analyzed oxide compounds, including average percentages, is presented in **Table 2**. Basic descriptive statistics for the elemental concentrations (in g/kg), such as median, mean, and standard deviation, are provided in Table 3; parameters that did not meet the minimum required number of measurements were excluded from the statistical summary in this table.

Table 2. XRF analysis results of 61 samples (%).

Compound	Minimum	Maximum	Median	Mean
CaO	17.00	82.10	59.00	59.23
SiO_2	7.030	47.40	20.60	20.38
Fe_2O_3	1.960	10.40	5.840	5.483
Al_2O_3	2.150	10.20	5.630	5.424
MgO	2.030	15.60	5.210	5.360
SO_3	0.218	19.10	0.960	1.793
Na_2O	0.178	1.070	0.474	0.491
TiO_2	0.236	0.940	0.562	0.599
K_2O	0.271	1.160	0.622	0.600
MnO	0.060	0.455	0.143	0.158
SrO	0.039	0.141	0.073	0.080
Cr_2O_3	0.048	0.414	0.132	0.149
P_2O_5	0.065	0.571	0.129	0.161
NiO	0.017	0.668	0.063	0.075
Cl	0.018	0.189	0.040	0.050
ZnO	0.000	0.068	0.029	0.030
CuO	0.005	0.022	0.015	0.015
ZrO_2	0.000	0.022	0.006	0.007

Co_2O_3	0.013	0.026	0.019	0.019
Y_2O_3	0.003	0.010	0.008	0.007
As_2O_3	0.000	0.014	0.010	0.008

Table 3. Summary of Basic Statistical Values for Element Analysis in 61 Samples (g/kg).

Elements	Number of detected points	Minimum	Maximum	Median	Mean	Std. Deviation	Skewness	Kurtosis	Coefficient of Variation (%)	Kolmogorov–Smirnov Test	Shapiro–Wilk Test
Ca	61	121.5	586.8	421.7	423.3	74.75	-0.606	3.548	17.66	0.2	0.003
Si	61	32.86	221.6	96.29	95.24	29.61	0.965	4.393	31.085	0.2	0.002
Fe	61	6.854	36.37	20.42	19.18	6.01	-0.097	0.058	31.321	0.017	0.113
Al	61	5.689	26.99	14.9	14.35	4.16	0.11	0.427	29.004	0.2	0.499
Mg	61	3.697	94.07	31.12	31.75	12.23	2.284	11.49	38.537	0	0
S	61	0.873	76.49	3.84	7.18	10.8	4.884	28.861	150.42	0	0
Na	61	0.66	3.969	1.758	1.82	0.647	0.839	1.335	35.552	0.2	0.428
Ti	55	1.414	5.634	3.368	3.589	1.038	0.258	-0.851	28.911	0.2	0.107
K	61	1.125	4.815	2.582	2.49	0.686	0.347	1.12	27.558	0.2	0.175
Mn	61	0.461	3.524	1.108	1.223	0.504	2.152	7.225	41.237	0.001	0
Sr	61	0.333	1.192	0.621	0.68	0.221	0.758	-0.288	32.426	0.031	0.002
Cr	40	0.165	1.416	0.452	0.508	0.244	1.483	3.548	48.009	0.186	0.001
P	61	0.142	1.246	0.282	0.351	0.205	2.264	6.271	58.47	0	0
Ni	60	0.131	5.248	0.495	0.589	0.675	5.882	39.697	114.584	0	0
Cl	53	0.175	1.89	0.398	0.496	0.335	2	5.117	67.535	0	0
Zn	59	0.104	0.542	0.237	0.241	0.102	1.027	0.973	42.266	0.2	0.001
Cu	23	0.042	0.177	0.117	0.12	0.03	-0.315	1.005	24.87	0.2	0.703
Zr	57	0.004	0.166	0.049	0.054	0.031	1.127	2.24	57.864	0.2	0.003
Co	12	0.046	0.091	0.066	0.069	0.015	0.26	-0.959	21.66	0.2	0.566
Y	10	0.01	0.038	0.031	0.028	0.009	-0.834	0.008	32.885	0.2	0.304
As	19	0.005	0.053	0.037	0.033	0.013	-0.784	-0.293	40.921	0.002	0.052

The average elemental concentrations in the samples ranged widely, from a minimum of 0.028 g/kg for Yttrium (Y) to a maximum of 423.3 g/kg for Calcium (Ca). The elements with the highest average concentrations, listed in descending order were: Ca (423.3 g/kg), Si (95.24 g/kg), Mg (31.75 g/kg), Fe (19.18 g/kg), Al (14.35 g/kg), and S (7.18 g/kg). The high concentrations of major elements like Ca, Si, Mg, Fe, and Al, and their corresponding oxides (CaO, SiO_2, MgO, Fe_2O_3, Al_2O_3), are consistent with the expected composition of construction and demolition waste, particularly components related to cement and raw materials (Stevulova et al. 2020).

The CaO/SiO_2 ratio in the samples (2.91, based on average oxide percentages) falls within the typical range for Portland cement (Type 1; 2.68-3.1), further indicating the significant influence of cementitious materials. The presence of other oxides and elements such as SO_3, P_2O_5, K_2O, and Cl is also consistent with the composition of cement and raw materials (Stevulova et al. 2020), aligning our results with findings from the literature.

Beyond the primary building materials, the elemental composition also suggests potential contributions from other anthropogenic sources, consistent with findings from global urban dust studies. Research has linked elements like

Co, K, Mn, and As to sources such as coal and wood burning (Kara, 2020); Cu and Zn to traffic emissions, vehicle wear and tear, gasoline use, and fossil fuel combustion (Kara, 2020; Sadeghdoust et al. 2020; Delibašić et al. 2020; Akhter and Madany, 1993; Manasreh, 2010); and Cr and Ni to industrial metallurgical processes and vehicle wear (Sadeghdoust et al. 2020; Delibašić et al. 2020; Ite et al. 2014; Akhter and Madany, 1993; Taşpınar and Bozkurt, 2018; Manasreh, 2010). Consistent with Azarmi and Kumar (2016) finding Si and Al as the main components in debris particles, our study also shows their high prevalence. In the context of this study, the use of heavy vehicles and machinery during extensive debris removal activities after the earthquake likely contributed significantly to the heavy metal pollution observed in the dust samples.

3.3. Correlation Analysis and Principal Component Analysis

A Pearson correlation analysis was conducted to investigate the relationships among the analyzed elemental concentrations in the 61 dust samples and assess the potential co-occurrence of elements originating from similar sources. The strength of relationships was classified based on Pearson correlation coefficients: very weak (0.00–0.25), weak (0.26–0.49), moderate (0.50–0.69), strong (0.70–0.89), and very strong (0.90–1.00) (Ersöz and Ersöz, 2022). Although the correlation analysis between elements has been presented in detail, correlations analysis alone may be limited to indicate common sources. For this reason, Principal Component Analysis (PCA) was also applied in this study to classify the elements in the dust samples (Ulutaş et al. 2025). The suitability of the dataset for PCA was examined using the Kaiser-Meyer-Olkin (KMO) and Bartlett's Sphericity tests. The KMO sample adequacy value was calculated as 0.758 (>0.50). Furthermore, it is recommended that future studies utilize different independent verification methods to support these findings and thus strengthen the interpretation of the sources.

The Pearson correlation coefficient matrix, presenting the relationships between all analyzed elemental pairs, is shown in Table 4. The analysis identified several significant correlations, indicating varying degrees of association between element concentrations. Four very strong correlations were observed: two negative correlations between Si and Ca (-0.97), and Al and Ca (-0.90); and two positive correlations between Al and Si (0.93), and Co and Cu (0.91). Additionally, several strong correlations were identified, including a negative correlation between Fe and Ca (-0.87), and positive correlations between Fe and Si (0.88), Al and Fe (0.82), and Y and Co (0.71). Other than these, 28 moderate correlations were detected, with Ti-Al (0.68) and Ni-Al (0.69) exhibiting the highest coefficients among them.

Table 4. Pearson Correlation Coefficients for Elements Identified in 61 Samples

	Ca	Si	Fe	Al	Mg	S	Na	Ti	K	Mn	Sr	Cr	P	Ni	Cl	Zn	Cu	Zr	Co	Y	As
Ca	1																				
Si	-0.97	1																			
Fe	-0.87	0.88	1																		

	As	Y	Co	Zr	Cu	Zn	Cl	Ni	P	Cr	Sr	Mn	K	Ti	Na	S	Mg	Al
As	-0.36	-0.29	-0.35	-0.56	-0.14	-0.26	0.02	-0.31	-0.27	-0.51	0.02	-0.05	-0.57	-0.51	-0.64	0.05	-0.55	-0.9
Y	0.37	0.27	0.36	0.56	0.11	0.28	-0.04	0.3	0.27	0.49	-0.1	0.07	0.61	0.54	0.66	-0.25	0.52	0.93
Co	0.5	0.31	0.4	0.5	0.05	0.21	-0.17	0.4	0.23	0.53	-0.28	-0.06	0.32	0.49	0.46	-0.34	0.56	0.82
Zr	0.36	0.24	0.21	0.59	0.1	0.33	-0.02	0.24	0.18	0.27	0	0.15	0.65	0.68	0.69	-0.21	0.27	1
Cu	0.02	0.31	0.45	0.19	-0.23	-0.11	-0.16	0.33	0.22	0.51	-0.39	0.01	-0.06	0.08	0.07	-0.32	1	
Zn	-0.1	-0.16	-0.56	-0.07	-0.14	-0.05	0.31	-0.16	-0.2	-0.4	0.6	-0.04	0.08	-0.23	0.04	1		
Cl	0.07	0.6	0.39	0.33	0.11	0.33	0.34	-0.08	-0.03	0.15	0.35	0.15	0.67	0.34	1			
Ni	0.1	0.15	0.28	0.61	0.4	0.23	-0.15	0.06	0.04	0.15	-0.11	0.16	0.31	1				
P	0.17	-0.43	0.24	0.23	0.09	0.34	0.26	0.02	0.2	-0.02	0.44	0.28	1					
Cr	-0.01	-0.38	0.36	-0.07	-0.04	-0.01	-0.01	0	-0.06	0.09	0.3	1						
Sr	-0.18	-0.64	-0.37	-0.26	0.16	0.21	0.34	-0.22	-0.05	-0.45	1							
Mn	0.14	0.26	0.56	0.55	-0.03	-0.14	-0.28	0.24	-0.06	1								
K	0.03	-0.63	-0.05	0.07	0.39	0.52	0.07	0.23	1									
Ti	0.18	-0.63	0.48	0.22	-0.1	0.3	-0.19	1										
Na	0.07	-0.44	-0.04	-0.04	-0.05	0.12	1											
S	0.11	-0.57	0.13	0.17	0.42	1												
Mg	-0.22	-0.43	0.91	0.21	1													
Al	0.31	-0.01	0.42	1														
	-0.12	0.71	1															
	0.28	1																
	1																	

These identified correlations provide insights into the potential sources contributing to the dust composition. The strong negative correlations between Ca (a major component of cement) and elements like Si, Al, and Fe (abundant in silicate and aluminosilicate minerals) are consistent with the inverse relationship expected between these primary constituents in construction materials. Conversely, the strong positive correlations among Si, Al, and Fe suggest their co-occurrence in silicate and aluminosilicate minerals present in the demolished structures. Furthermore, the correlation analysis revealed relationships potentially indicative of specific asbestos types, aligning with interpretations from the elemental analysis. Medium to strong positive correlations between Si and elements like Fe, Mg, and Na suggest the possible presence of serpentine and amphibole asbestos types, such as chrysotile, anthophyllite, amosite, and crocidolite. The very strong negative correlation between Ca and Si, and

the strong negative correlation between Ca and Fe, might indicate the limited presence or absence of tremolite and actinolite asbestos among the identified silicate/aluminosilicate-rich particles.

Beyond the primary components of cement and potential asbestos, the correlation analysis also suggests the influence of other sources of contamination. Positive correlations like Co-Cu and Y-Co, along with several moderate correlations, point towards contributions likely originating from demolition activities, materials from vehicles operating in the debris area, and various other materials in the demolished buildings, such as household contents. These relationships support the interpretation of significant anthropogenic influences on the elemental composition of the earthquake-generated dust.

Based on the Kaiser criterion (eigenvalue > 1) and using the Varimax rotation method, the analysis revealed a robust 6-component structure explaining 71.72% of the total variance. This ratio shows that the majority of the data is successfully represented for identifying the sources of earthquake dust.

Table 5: Principal Component Analysis (PCA) results and attributed possible sources affecting the collected samples.

Parameters	PC1	PC2	PC3	PC4	PC5	PC6
Si	0.957					
Ca	-0.942					
Al	0.932					
Fe	0.808					
Na	0.796					
K	0.709					
Ti	0.485					
Sr		0.787				
S		0.742				
Mg		-0.561				
Mn						
Cr			0.698			
Zr			0.632			
Cl			-0.6			
Y				-0.837		
Ni				0.818		
Cu					0.796	
Zn					0.681	
P					0.634	
Co						-0.738
As						0.698
Sum of Squared Loadings	5.43	2.36	1.92	1.9	1.8	1.41
Variance Percent	25.86	11.23	9.13	9.03	8.55	6.71

Cumulative Percent	25.9	37.1	46.2	55.2	63.8	70.5

Principal component 1 (PC1) showed 25.86 % of the total data variance. PC1 was loaded very heavily with Si (0.957), Al (0.932), Fe (0.808), Na (0.796), and K (0.709) positively, while Ca (-0.942) loaded negatively. PC1 reflects Si- and Al-rich construction debris contrasted with Ca-rich materials (Table 5). The CaO/SiO_2 ratio is also important for cement quality (Stevulova et al. 2020). Natural resources can also have an effect due to the elements that are abundant in the soil. Therefore, PC1 is most likely associated with construction waste and the earth's crust. PC2 accounted for 11.23% of the total data variance. PC2 was heavily loaded with Sr (0.787), S (0.742) positively, while Mg (-0.561) loaded negatively. Sr has different absorption rates from cement-based materials (Wieland et al. 2008). Sr and Mg are the most abundant elements in the Earth's crust (Nedobukh and Semenishchev, 2019). However, since they behave in opposite ways, they are not expected to represent the same source. S represents gypsum ($CaSO_4$) and plaster materials used in the interior walls of buildings. This group has separated from coarse concrete to form a finer powder phase (Lancia et al. 2000). PC2 can serve as an indicator of mixed sources, gypsum, plaster materials, and the earth's crust. PC3 specified 9.13% of the total data variance. PC3 was loaded with Cr (0.698), Zr (0.632), Cl (-0.600). Cr is commonly used in steel alloys and chromium coatings (Fuge, 2012), while Zr is widely applied in ceramic coatings (Long et al. 2016). PC3 may be more associated with industrial products and chlorine decomposition. PC4 showed 9.03 % of the total data variance. PC4 was loaded with Ni (0.818) and Y (-0.837). Previous studies have reported that fuel combustion, engine wear, and industrial activities such as alloying and welding are the main sources of Ni (Kumari et al. 2021; Xu et al. 2017). Its contrasting action with yttrium (Y) indicates that rare earth elements and industrial metals in the debris originated from different sources. PC4 can be classified in relation to special alloys and traffic. PC5 and Factor 6 explain 8.55% and 6.71% of the total variance, respectively. Factor 5 is charged by Cu (0.796), Zn (0.681), P (0.634). In buildings, the most common sources of copper (Cu) are electrical cables, zinc (Zn) are galvanized sheets (roofing/pipes), and phosphorus (P) are organic wastes in sewage systems. PC5 may be more associated with plumbing, electrical and electronic waste, and urban infrastructure waste. PC6 is dominated by As (0.698) and Co (-0.738). Although both are toxic, the contrasting interaction between them suggests they originate from different sources. This is the most critical finding from an environmental and public health management perspective because it has emerged as a dominant factor, isolated from other heavy metals. This situation can be considered a hidden danger. Therefore, PC6 is most likely associated with toxic risk.

3.4. Determination of Pollution Levels Using Enrichment Factor and Ecological Risk Index

To evaluate the enrichment of specific elements in debris dust relative to background soil composition and to evaluate the influence of natural and anthropogenic sources, the Enrichment Factor (EF) was calculated using Al as the reference element (Equation 1). The calculated EF values were visualized using a Box-Whisker plot in Figure 3. The box edges represent the 25th and 75th percentiles; the central line indicates the median (50th percentile), and “X” denotes the mean.

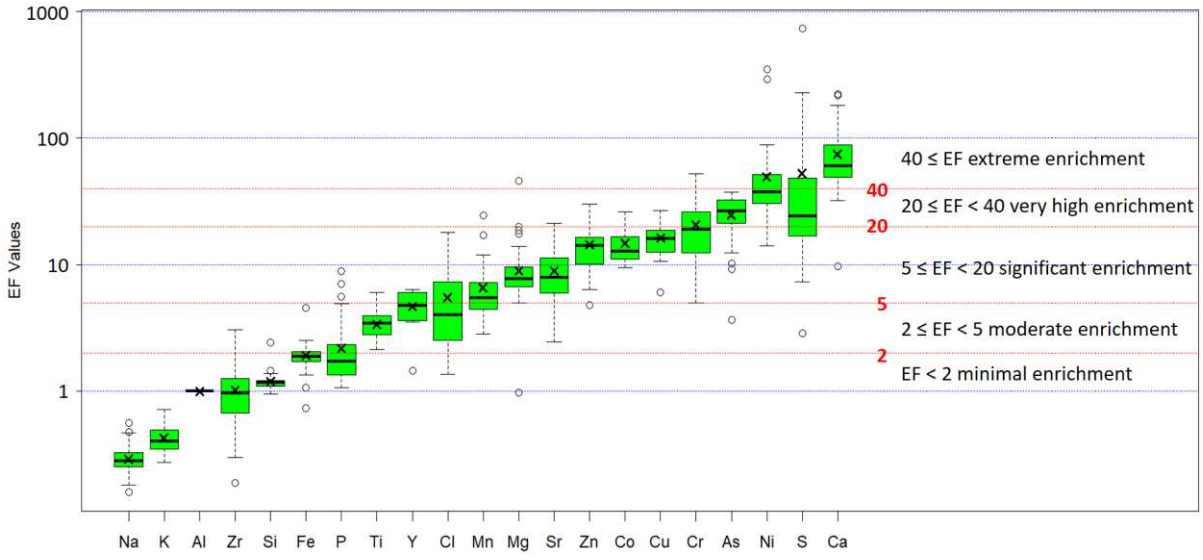


Fig. 3 EFs calculated for the elements identified in 61 samples, with the y-axis shown on a logarithmic scale

The interpretation of EF values enabled the identification of source contributions and the extent of anthropogenic impact. Elements with minimal enrichment (EF < 2), specifically Na, K, Al, Zr, Si, and Fe, suggest they primarily originate from the geological composition of the study area. While some of these elements are present in concrete, their low EF values are likely due to their significant presence in background soil. Elements with moderate enrichment (2 ≤ EF < 5), including P, and Ti, indicate potential influence from non-soil sources. Elements exhibiting significant enrichment (5 ≤ EF < 20), such as Cl, Mn, Sr, Mg, Zn, Co, and Cu, strongly suggest human-induced pollution in the study area. High enrichment (20 ≤ EF < 40) was observed for Cr, and As while Ni, S, and Ca displayed very high enrichment (EF ≥ 40). The high EF values for Ni, S, and Ca are strong indicators of significant anthropogenic origins. While Ca is a major component of concrete, its high EF highlights the substantial contribution of this source in the dust. Collectively, the high EF values for multiple elements point towards significant anthropogenic pollution in the study area, likely attributable to construction waste, heavy vehicles used in demolition and debris removal, and potentially other materials present in the structures affected by the earthquake. Additionally, given the composite nature of the samples, other sources mixed with debris from various household materials may also contribute to the observed enrichment.

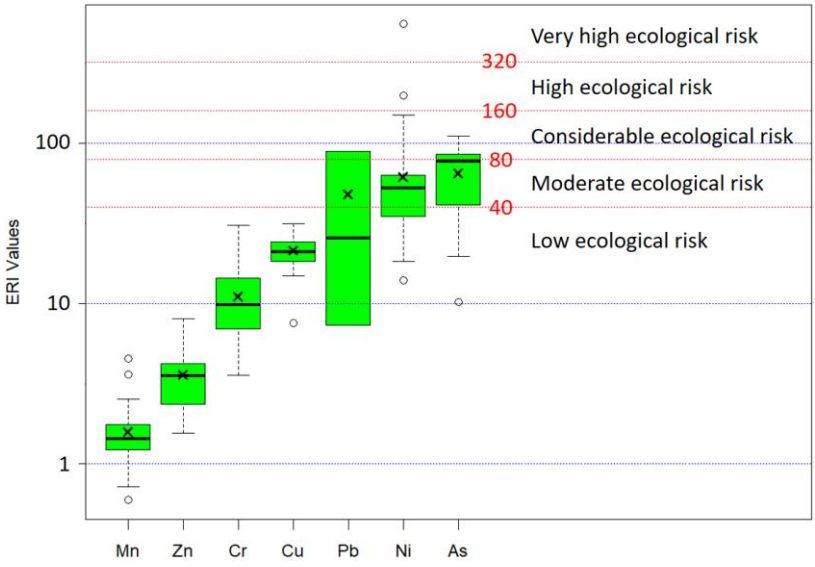


Fig. 4 ERFs for Zn, Mn, Cr, Cu, Ni, and As, with the y-axis shown on a logarithmic scale

To assess the pollution levels of dust accumulated on building foundations following demolition and debris removal, Ecological Risk Factor (ERF) (Figure 4) and Ecological Risk Index (ERI) analyses were applied (Hakanson, 1980). The average ERF values for Cu, Cr, Zn, and Mn were calculated as 21.45, 11.05, 3.60, and 1.58, respectively. In contrast, the ERF values for As and Ni were notably higher, at 68.22 and 62.69. For As, moderate ecological risk ($40 \leq ERF < 80$) was identified at seven sampling points, and considerable ecological risk ($80 \leq ERF < 160$) at 8 points. For Ni, 35 samples indicated moderate risk, four samples considerable risk, one sample high risk ($160 \leq ERF < 320$), and one sample very high ecological risk ($ERF \geq 320$). Overall, the ERF values for Zn, Cr, Mn, and Cu remained below 40, indicating low potential ecological risk from these specific elements across most samples. Based on the average concentrations, the potential ecological risk values for elements As, Ni, Cu, Cr, Zn, and Mn indicated a moderate level of risk overall for the study area.

The ERI was calculated as 168.59 by summing the risk factor values of Zn, Mn, Cr, Cu, Ni, and As, which were the elements for which ecological risk factors were determined. This ERI value indicates a moderate level of ecological risk in terms of pollution for the study area, as it falls within the range of 150 to 300.

Although these methods were not specifically developed for application in post-earthquake regions, they were used in this study to assess pollution levels. The results demonstrate that the EF and ERI methods can be applied to post-earthquake study areas using composite sampling due to their ability to reflect the effects across the entire sampling area. However, a critical approach may be necessary as EF and ERI were developed for natural soils and therefore have some limitations in mixed construction and demolition waste. Therefore, EF and ERI may not be considered absolute risk indicators, but they may use as rather comparative tools for screening and spatial assessment. To support this approach, the results of these methods were visualized using maps in order to strengthen the interpretations.

3.5. Analysis Results of Asbestos and Fibrous Structures

Analysis for fibrous structures, including potential asbestos presence, was conducted on a total of 23 selected dust samples. Samples were collected by adhering dust onto 2.5-mm diameter carbon adhesive tapes. Using Scanning Electron Microscopy coupled with Energy-Dispersive X-ray Spectroscopy (SEM-EDS), fifty distinct points were examined per sample to assess both particle dimensions and chemical composition. An initial screening process was implemented based on dimensional criteria on dimensional criteria (AÇİSGUR, 2019). Particles or fibers identified with a length exceeding 5 µm, a width less than 3.5 µm, and a length-to-width ratio greater than 3:1 were selected. In this initial scan using SEM technology, a total of 1,415 particles or fibers were detected in all 23 samples at dimensional ratios and their chemical composition was subsequently determined using EDS. After the dimensional and chemical screening, particles lacking detectable silicon (Si) levels were excluded. This exclusion was based on Si being a key component of the silicate minerals that form asbestos. This filtering step resulted in a reduced set of 1370 fibrous structures retained for further chemical characterization. These selected structures were then analyzed by EDS to determine their elemental composition, considering the typical mineral profiles of various asbestos types (Table 1). Analysis of the elemental composition within this set of 1,370 fibrous structures revealed varying distributions of key elements associated with asbestos minerals. Specifically, magnesium (Mg) was detected in 1148 particles, iron (Fe) in 669, sodium (Na) in 79, and calcium (Ca) was present in all 1370 particles. The co-occurrence of Ca, Mg, and Fe, observed in 669 particles, suggests potential overlap with the elemental profiles of multiple asbestos mineral types. The prevalence of Mg detection is particularly noteworthy, given that chrysotile, the most common type of asbestos, contains Mg as a primary component.

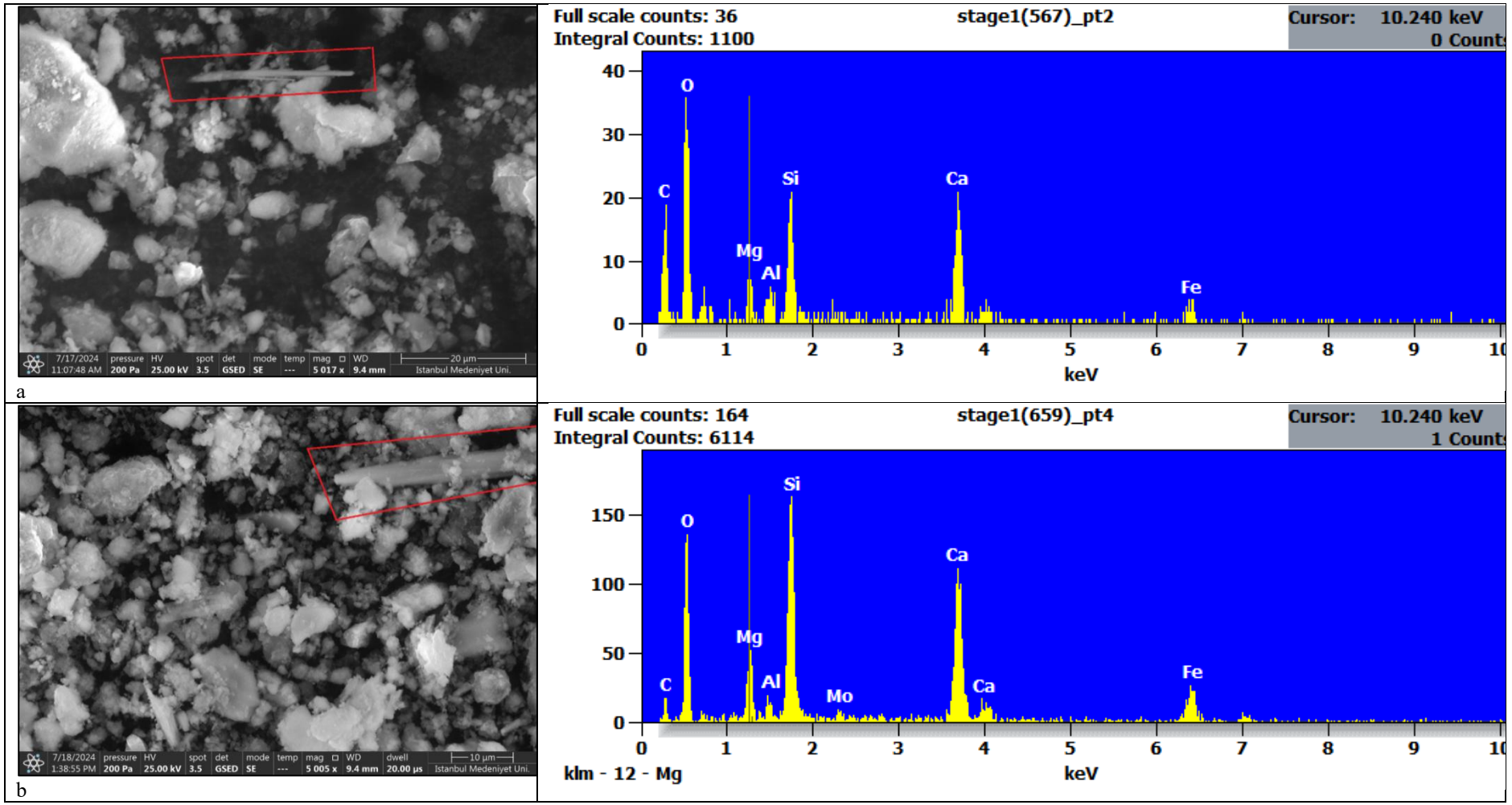
Following the initial identification of fibrous structures based on dimensional criteria and Si presence, a more comprehensive evaluation was deemed necessary since visual examination revealed that not all these structures exhibited the characteristic fibrous morphology of asbestos. Therefore, a rigorous assessment incorporating dimensional, chemical, and morphological characteristics was performed. Combining morphological (SEM) and chemical (EDS) analyses proved crucial for accurate and definitive classification, as visual similarity alone was insufficient.

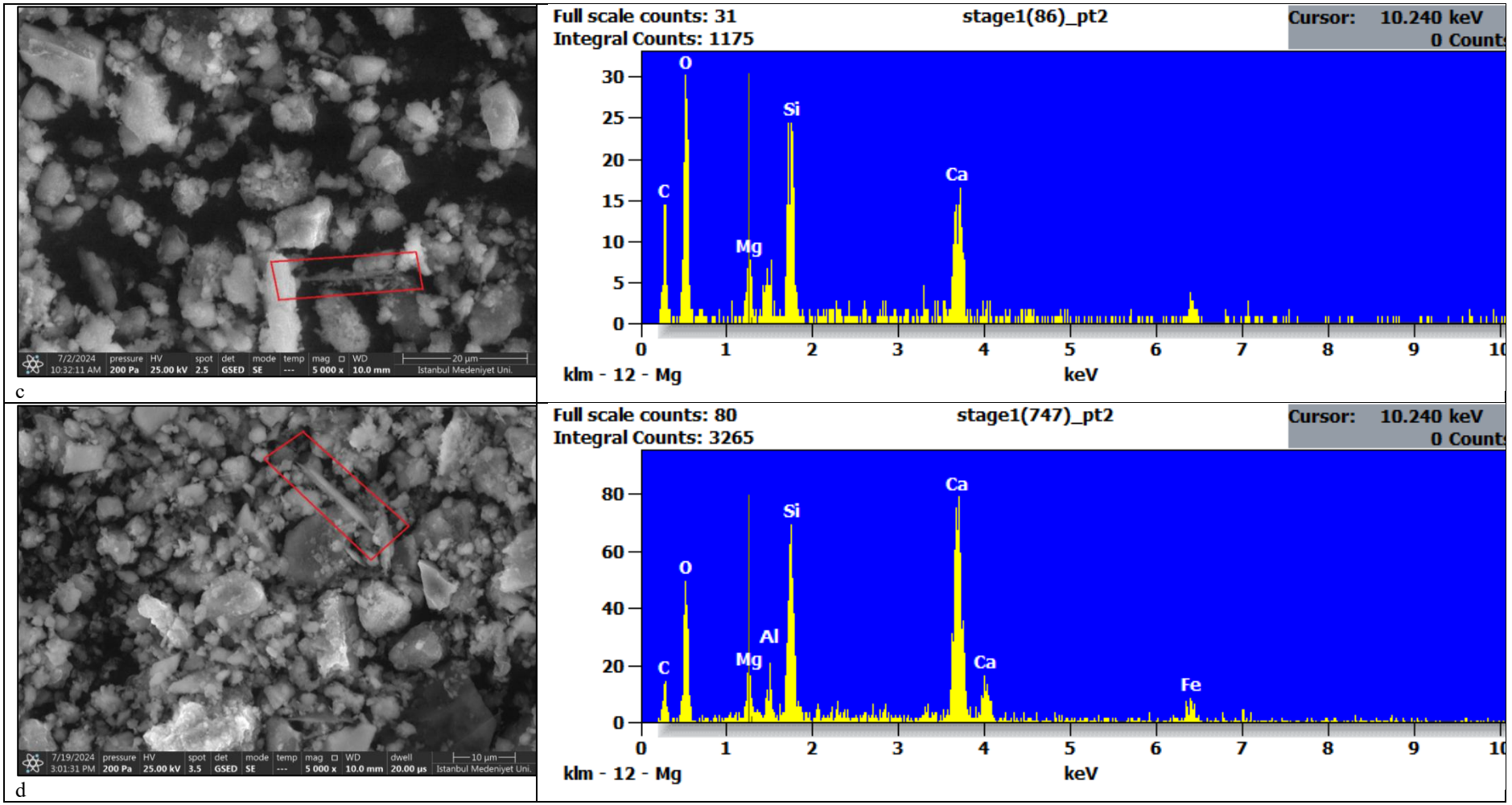
Table 6. The chemical composition (%, w/w) of the fibrous structures identified as asbestos.

Figure No.	C	O	Mg	Al	Si	Ca	Fe	Mo	S	K	F
8a	20.97	56.83	2.99	2.19	6.75	6.61	3.65				
8a	17.70	61.45	4.12		9.50	7.23					
9b	6.57	51.37	5.50	1.37	14.66	12.57	6.69	1.28			
10c	20.91	57.25	4.10		9.30	8.44					
11d	10.43	49.86	3.00	1.58	11.39	19.30	4.44				
12e	7.10	58.02	4.78	2.25	11.92	11.81	4.11				
13f	11.05	59.79	2.35	3.80	9.18	11.04	2.19			0.60	
14g	6.15	55.76	7.24	1.69	13.94	11.57	2.59	1.07			
15h	6.56	56.45	5.89	1.86	11.29	13.97	3.98				
16i	19.05	53.14	5.12	1.10	10.35	6.89	4.35				
17j	6.09	58.04	15.13	0.51	11.91	5.28	2.35				0.69

17j	12.54	59.12	9.22	0.66	6.90	9.92	1.63

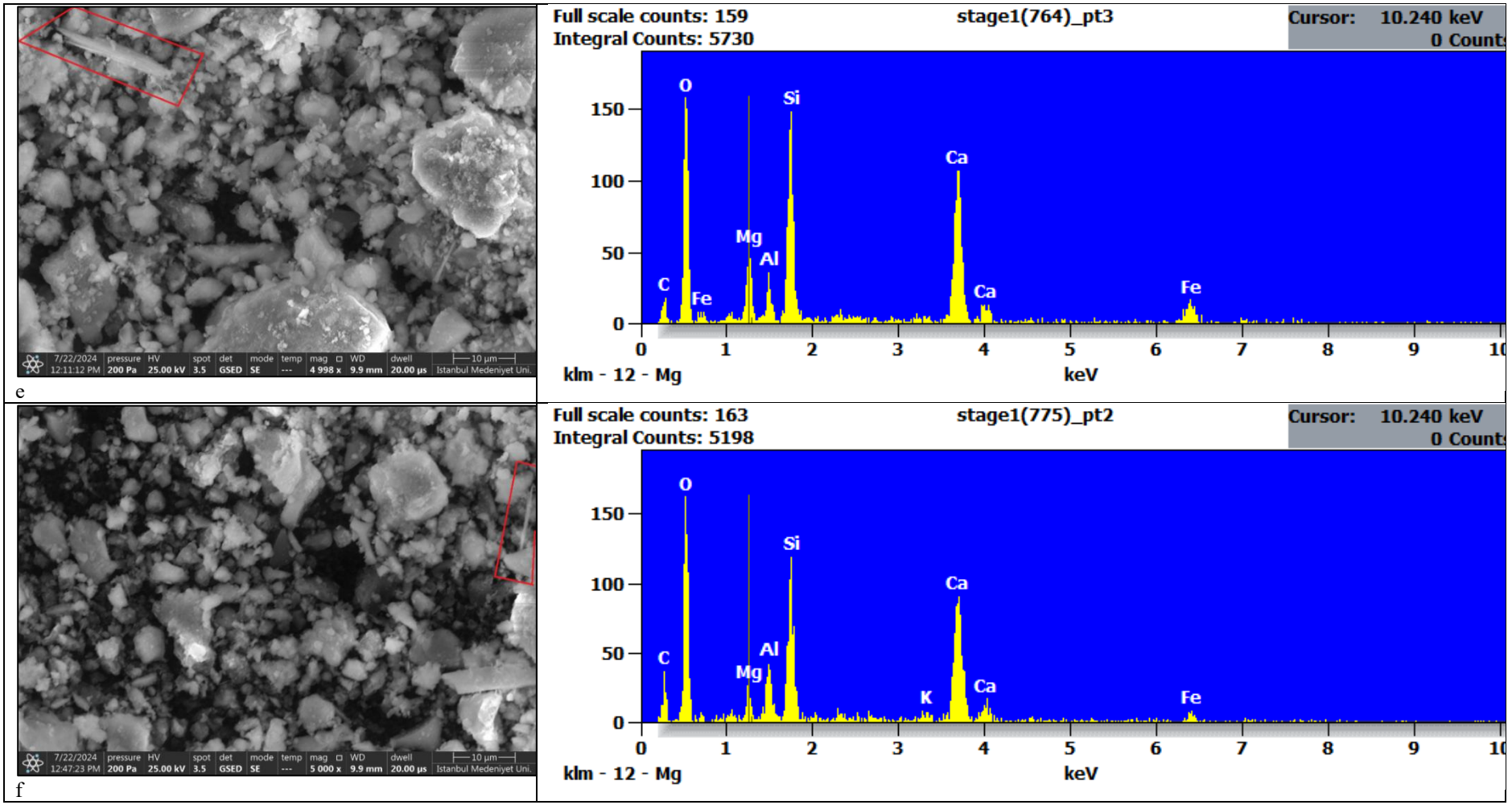
Table 6 presents the chemical composition (by weight %) of these selected particles identified as asbestos, while their SEM images, illustrating key morphological features, are shown in Figure 5a-j. Visual assessment frequently revealed characteristic features consistent with asbestos fibers, such as frayed or split ends, which are apparent in numerous figures. Fibers were also observed in bundled or clustered arrangements, sometimes appearing thicker, as seen in Figure 5b, d, g, and j. Additionally, as seen in Figure 5j, asbestos fibers are flexible and can be bent. Particles displaying clear bundling and distinct frayed ends (Figure 5h) were confidently identified as asbestos. Similarly, the presence of frayed edges and ends on fine fibers, coupled with compatible chemical compositions (Figure 5a, c, d, and f), increased the likelihood of their identification as asbestos. Although some structures showed visual similarities to fibrous asbestos, such as in Figure 5i where coarser fragmentation and thicker appearance raised doubts, it was ultimately identified as due to its frayed ends and general chemical composition.

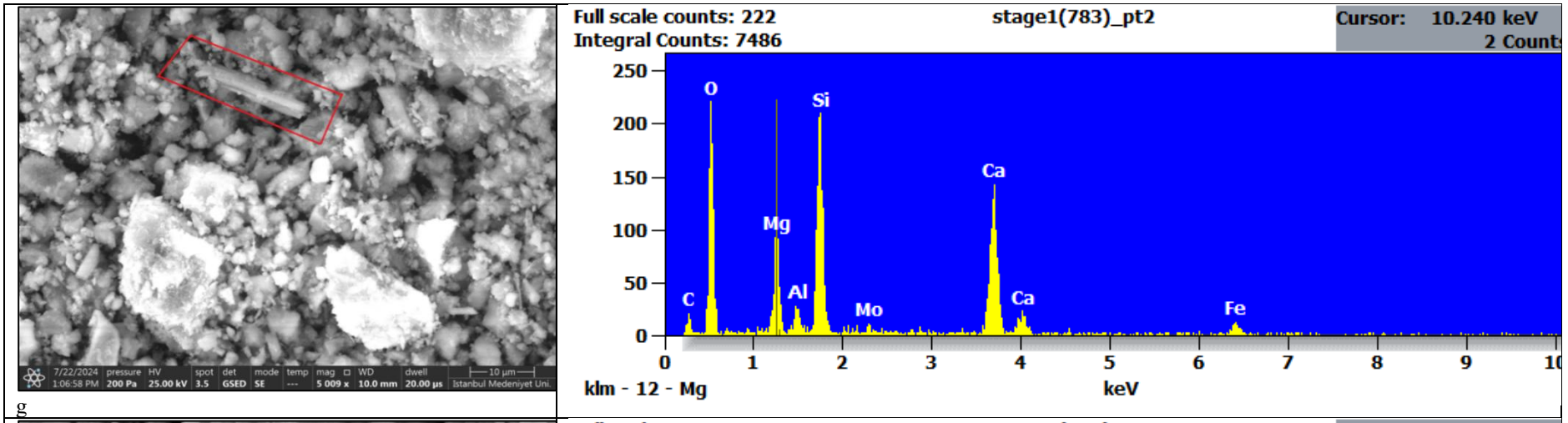

7/17/2024 11:07:48 AM pressure 200 Pa HV 25.00 kV spot 3.5 det GSED mode SE temp --- mag 5 017 x WD 9.4 mm 20 µm Istanbul Medeniyet Uni.
a
Full scale counts: 36
Integral Counts: 1100
stage1(567)_pt2
Cursor: 10.240 keV
0 Count
O
C
Si
Ca
Mg
Al
Fe
keV
7/18/2024 1:38:55 PM pressure 200 Pa HV 25.00 kV spot 3.5 det GSED mode SE temp --- mag 5 005 x WD 9.4 mm dwell 20.00 µs 10 µm Istanbul Medeniyet Uni.
b
Full scale counts: 164
Integral Counts: 6114
stage1(659)_pt4
Cursor: 10.240 keV
1 Count
O
Si
Ca
C
Mg
Al
Mo
Ca
Fe
klm - 12 - Mg
keV


7/2/2024 10:32:11 AM pressure 200 Pa HV 25.00 kV spot 2.5 det GSED mode SE temp --- mag 5 000 x WD 10.0 mm 20 µm İstanbul Medeniyet Uni.
Full scale counts: 31
Integral Counts: 1175
stage1(86)_pt2
Cursor: 10.240 keV
0 Count
O
Si
Ca
C
Mg
30
25
20
15
10
5
0
0 1 2 3 4 5 6 7 8 9 10
klm - 12 - Mg
keV
7/19/2024 3:01:31 PM pressure 200 Pa HV 25.00 kV spot 3.5 det GSED mode SE temp --- mag 5 000 x WD 10.0 mm dwell 20.00 µs 10 µm İstanbul Medeniyet Uni.
Full scale counts: 80
Integral Counts: 3265
stage1(747)_pt2
Cursor: 10.240 keV
0 Count
Ca
Si
O
Al
Mg
C
Ca
Fe
80
60
40
20
0
0 1 2 3 4 5 6 7 8 9 10
klm - 12 - Mg
keV

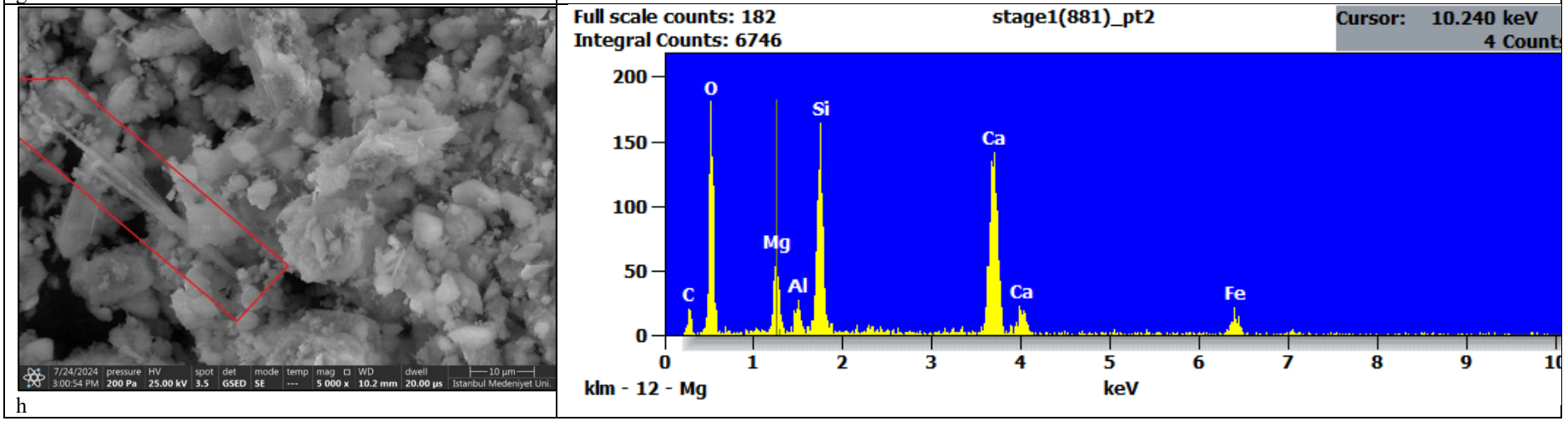
c

d

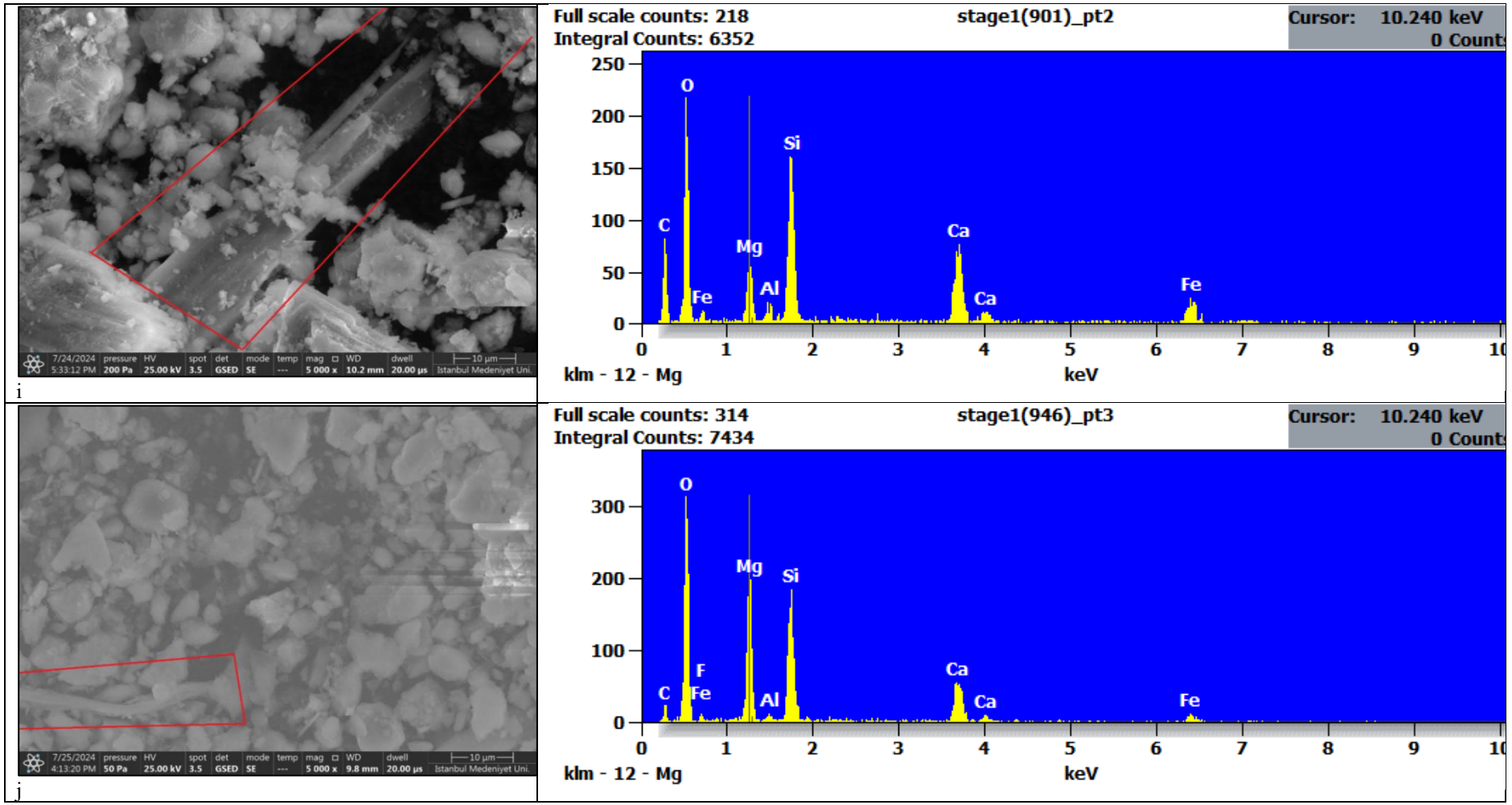

7/22/2024 12:11:12 PM
pressure 200 Pa
HV 25.00 kV
spot 3.5
det GSED
mode SE
temp ---
mag 4 998 x
WD 9.9 mm
dwell 20.00 µs
10 µm
İstanbul Medeniyet Uni.
Full scale counts: 159
Integral Counts: 5730
stage1(764)_pt3
Cursor: 10.240 keV
0 Count
O
Si
Ca
Mg
Al
C
Fe
Ca
Fe
klm - 12 - Mg
keV
e
7/22/2024 12:47:23 PM
pressure 200 Pa
HV 25.00 kV
spot 3.5
det GSED
mode SE
temp ---
mag 5 000 x
WD 9.9 mm
dwell 20.00 µs
10 µm
İstanbul Medeniyet Uni.
Full scale counts: 163
Integral Counts: 5198
stage1(775)_pt2
Cursor: 10.240 keV
0 Count
O
Si
Ca
C
Al
Mg
K
Ca
Fe
klm - 12 - Mg
keV
f


7/22/2024 1:06:58 PM pressure 200 Pa HV 25.00 kV spot 3.5 det GSED mode SE temp --- mag 5 009 x WD 10.0 mm dwell 20.00 µs 10 µm Istanbul Medeniyet Uni.
Full scale counts: 222
Integral Counts: 7486
stage1(783)_pt2
Cursor: 10.240 keV
2 Count
O
Si
Ca
Mg
C
Al
Mo
Ca
Fe
klm - 12 - Mg
keV

g


7/24/2024 3:00:54 PM pressure 200 Pa HV 25.00 kV spot 3.5 det GSED mode SE temp --- mag 5 000 x WD 10.2 mm dwell 20.00 µs 10 µm Istanbul Medeniyet Uni.
Full scale counts: 182
Integral Counts: 6746
stage1(881)_pt2
Cursor: 10.240 keV
4 Count
O
Si
Ca
Mg
C
Al
Ca
Fe
klm - 12 - Mg
keV

h



427 **Fig. 5** SEM-EDS images and of the fibrous structures identified as asbestos (a–j).

428

Following this comprehensive assessment, only a very small proportion of the analyzed objects-10 out of 1,370-were identified as asbestos, highlighting the limited prevalence of asbestos in the studied sample. The confirmed asbestos fibers were detected at 6 out of the 61 sampling locations, with their occurrences ranging from one to four fibers per location. The spatial distribution of all fibrous structures (represented by green circles) and the confirmed asbestos fibers (represented by red triangles) across the sampling locations is illustrated in Figure 6. The highest number of detected asbestos fibers was observed at a sampling point located in an area characterized by 2–3-story old informal housing. Notably, no significant correlation was found between the total number of fibrous structures identified and the presence of confirmed asbestos fibers. Only 10 asbestos fibers were detected in the study. Therefore, with such a small number of fibers, spatial distribution and precise source identification would be quite limited. Furthermore, factors such as wind effects or mechanical activity should be considered, and it should be thought that different sources may have influenced the spatial distribution of the fibers. Therefore, more comprehensive and detailed studies are needed regarding the spatial distribution and source analysis of asbestos fibers.

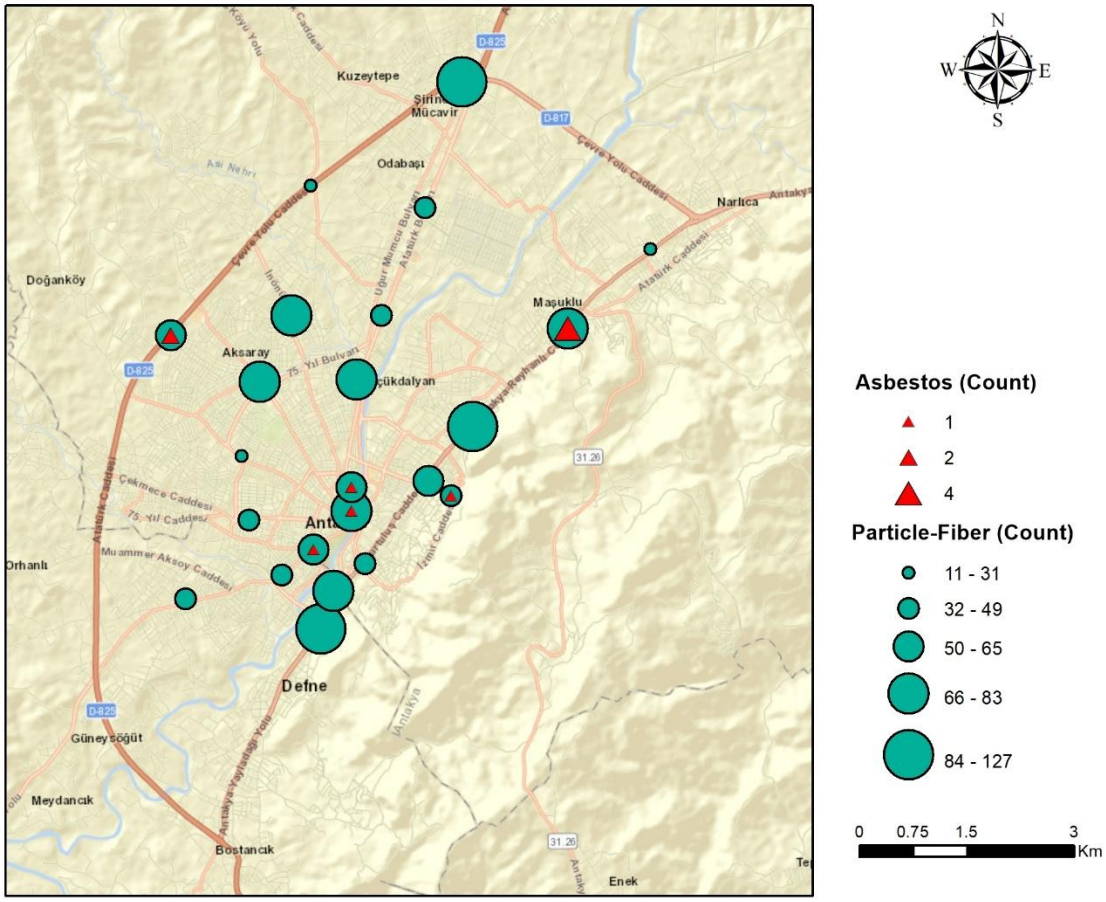


Fig. 6 Distribution map of asbestos and fibrous particles identified in 23 samples.

3.6. Distribution Maps of Analyzed Parameters and Enrichment Factors

The spatial distribution of elemental concentrations across the sampling points was evaluated to identify potential source influences. This analysis considered the general age of surrounding demolished buildings (broadly categorized as old or new based on pre-earthquake Google Earth imagery) and proximity to main traffic arteries as potential factors influencing concentration variations. The comprehensive spatial distribution maps for each analyzed parameter are presented in Figure 7, visually illustrating these patterns.

Si, Fe, Al, and Cr exhibited their highest concentrations concurrently at Sampling Point 28 (see Figure 1 for sampling locations), located on a main road passing through the city, while Ca and S showed their lowest concentrations at the same point. In contrast, the lowest Si, Fe, and Al concentrations were observed together at Point 12, characterized by older 3–4 storey buildings. The highest Mg concentration and the lowest concentrations of Na, Ti, K, Sr, and Zn were recorded at Point 41, situated on a road in the eastern part of the city with limited demolition activity. The lowest Mg concentration, coupled with the highest Cu concentration, was found at Point 40, located on a bridge behind an industrial site with a few low-rise buildings. High S and low P concentrations were noted at Point 2, where a new 7–8 storey building was located. High Na and K concentrations were measured at Point 19, which consisted of older informal settlements of 2–3 storeys. High Ti and Y concentrations were found at Point 60, near older 5-storey buildings. Other elements, such as Mn (Point 9, an old 6-storey building site), Sr (Point 20, old 4–5 storey buildings), and P (Point 54, old historical 1–2 storey houses), also exhibited their highest concentrations at specific locations associated with older structures. Ni showed both its highest (Point 26) and lowest (Point 46) concentrations near recently constructed 5–6 storey and 7–8 storey buildings, respectively. The highest and lowest Cl concentrations were detected at sampling points located at intersections with 5–6-storey old buildings and 2–3-storey old buildings, respectively. The highest Zr concentration was found at Sampling Point 23, located at an intersection along a major road outside the city to the northwest, whereas the lowest Zr concentration was observed at Sampling Point 10, where both 2–3-storey old buildings and 5–6-storey new buildings were present. For Co, the highest and lowest concentrations were recorded at Sampling Points 49 (along a street opposite a park, with 6–7-storey old buildings) and 32 (with 4–5-storey old buildings), respectively. The highest Zn concentration was measured at Sampling Point 8, where mixed old and new 4–5-storey buildings were located. The lowest Cr concentration was observed at Sampling Point 6 (4–5-storey old buildings), while the lowest Cu and Y concentrations were detected at Sampling Points 58 (6–7-storey new buildings) and 26 (5–6-storey new buildings), respectively.

Spatial analysis revealed that variations in elemental concentrations were influenced by both the age of demolished structures and the proximity of sampling points to traffic arteries. Higher concentrations of elements such as P, Y, Co, Na, K, and Sr were generally associated with areas characterized by older buildings, whereas Si, Fe, Al, and Mg concentrations were elevated near main traffic routes. For example, Si, Fe, Al, and Cr reached peak levels at a sampling point along a major city road, whereas Ca and S were lowest at the same location. Conversely, the lowest concentrations of Si, Fe, and Al were found at a point with older structures, and high Mg but low Na, Ti, K, Sr, and Zn concentrations were recorded in an eastern area with limited demolition activity.

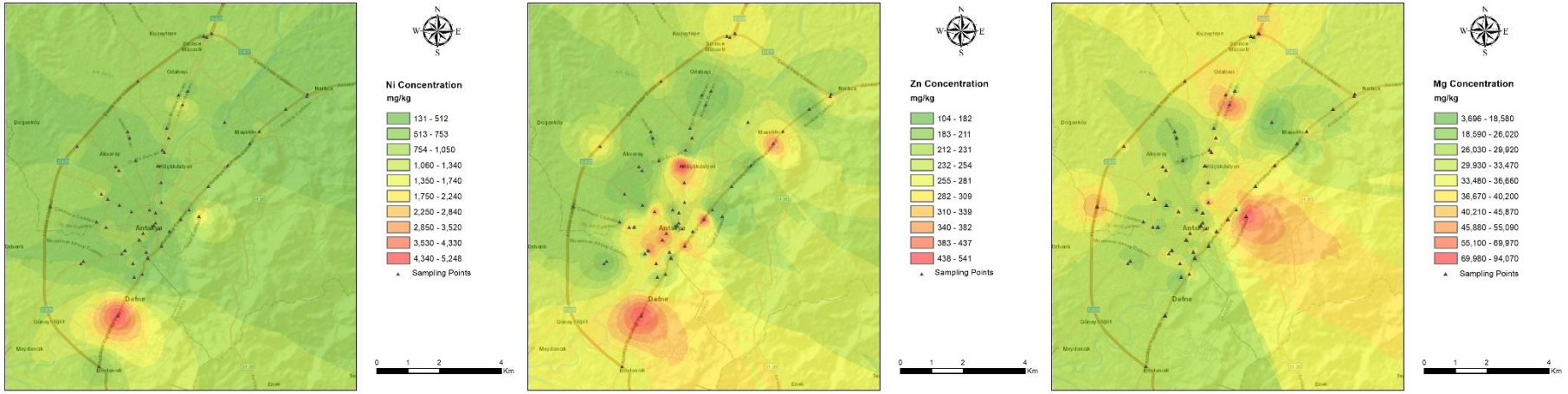
Distribution maps further indicated distinct spatial patterns. Zn, Ni, Mg, and P concentrations were dominant in the city's southern parts, with Mg and P also elevated in the city center and decreasing southeastward. Ti and Cl

concentrations were notably higher in the northwest, whereas Al, Fe, Mn, Na, and Si showed higher levels in the north, with Al and Fe also elevated in the southwest. Cr and Zr were lower in the south and southeast, though Zr was locally high in the city center. As and Ca concentrations were elevated in the southwest and northeast, while Co, Cu, and Y were more influential in the north and northeast. These findings reflect a complex distribution of elements driven by multiple anthropogenic and environmental factors in the post-earthquake urban environment.

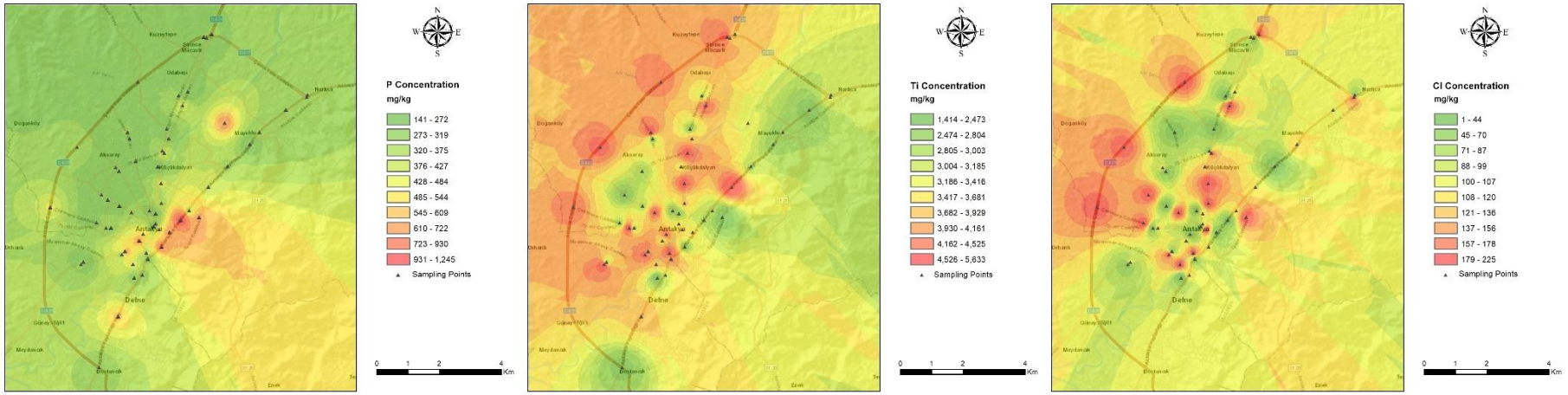
In addition to the concentration-based distribution maps, distribution maps based on Enrichment Factor (EF) values were generated to assess the degree of elemental enrichment relative to background levels (Figure 8). EF maps are particularly useful for identifying significant anthropogenic contamination. Maps were prepared for elements with an average EF value greater than 5, indicating significant enrichment. Ordered by increasing average EF values, these elements were Sr (5.53), Cu (5.86), Co (6.35), Cl (11.21), Cr (11.57), Ni (19.35), Ca (36.43), As (45.90), and S (96.75).

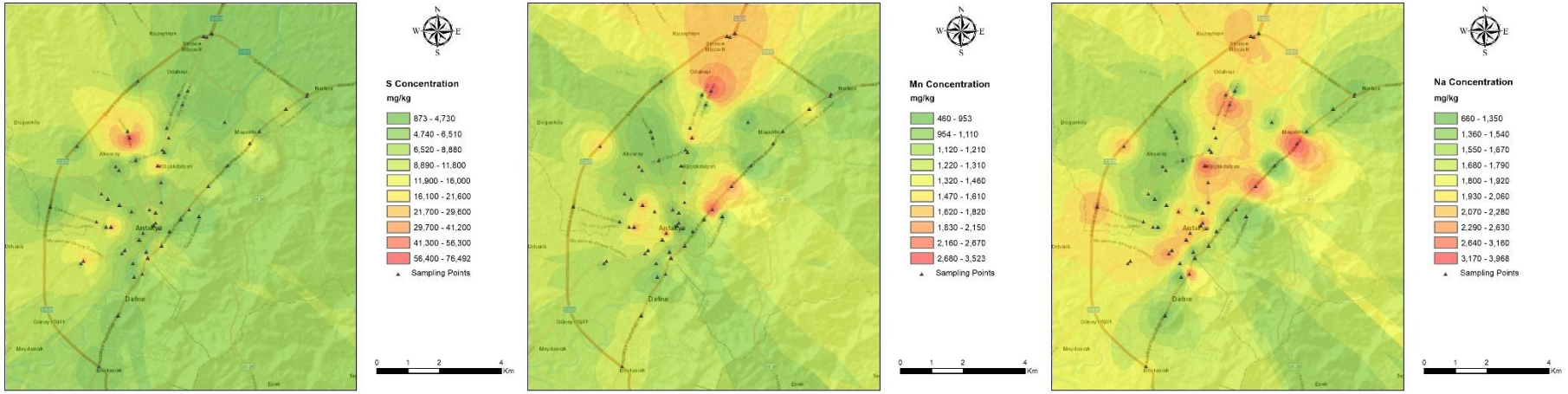
For Sr, relatively low EF values were observed in the city center, north, south, and west, while higher values appeared in the east and northwest. Cu exhibited a similar distribution but showed more clustered moderate enrichment, with significant EF values across most areas except for some points north of the center and in the south. Co displayed significant enrichment citywide, indicating widespread contamination relative to background levels. Zn also exhibited considerable enrichment, although high values were confined to specific areas. Cl showed moderate EF values in the west and northwest, rising to very high levels in the northeast and parts of the city center, with generally significant enrichment elsewhere. Ni EF values were particularly high to very high in the southern part of the city. Ca EF values ranged from very high to extremely high, especially in the west and east. As EF values were predominantly extremely high, with only a limited area in the city center showing lower enrichment. Similarly, S exhibited generally extremely high EF values across the city, with a few locations displaying very high enrichment.

505

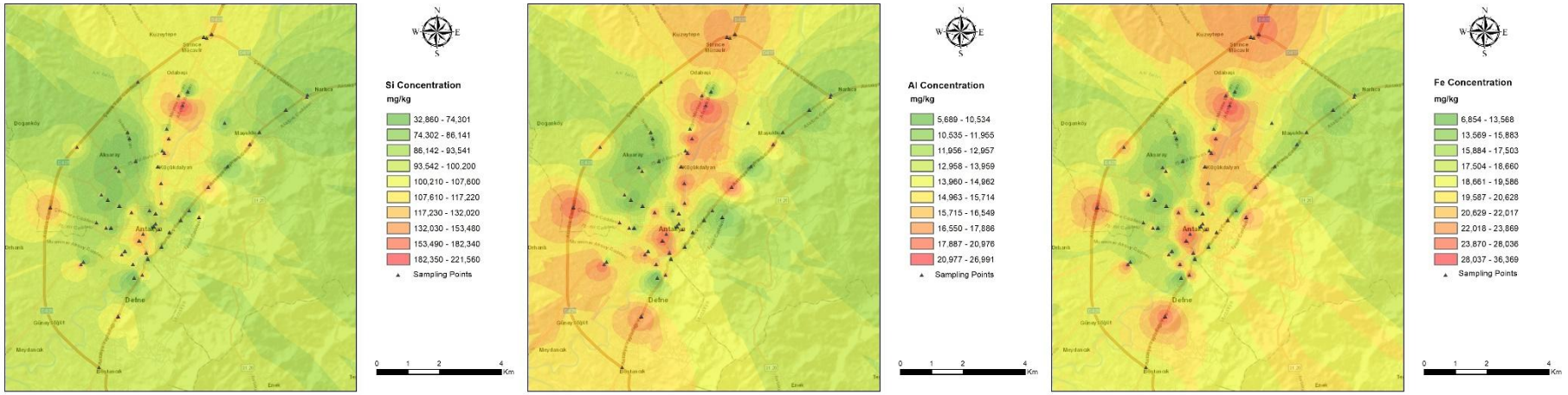

Ni Concentration
mg/kg
131 - 512
513 - 753
754 - 1,050
1,060 - 1,340
1,350 - 1,740
1,750 - 2,240
2,250 - 2,840
2,850 - 3,520
3,530 - 4,330
4,340 - 5,248
Sampling Points
Zn Concentration
mg/kg
104 - 182
183 - 211
212 - 231
232 - 254
255 - 281
282 - 309
310 - 339
340 - 382
383 - 437
438 - 541
Sampling Points
Mg Concentration
mg/kg
3,696 - 18,580
18,590 - 26,020
26,030 - 29,920
29,930 - 33,470
33,480 - 36,660
36,670 - 40,200
40,210 - 45,870
45,880 - 55,090
55,100 - 69,970
69,980 - 94,070
Sampling Points
0 1 2 4 Km

506


P Concentration
mg/kg
141 - 272
273 - 319
320 - 375
376 - 427
428 - 484
485 - 544
545 - 609
610 - 722
723 - 930
931 - 1,245
Sampling Points
Ti Concentration
mg/kg
1,414 - 2,473
2,474 - 2,804
2,805 - 3,003
3,004 - 3,185
3,186 - 3,416
3,417 - 3,681
3,682 - 3,929
3,930 - 4,161
4,162 - 4,525
4,526 - 5,633
Sampling Points
Cl Concentration
mg/kg
1 - 44
45 - 70
71 - 87
88 - 99
100 - 107
108 - 120
121 - 136
137 - 156
157 - 178
179 - 225
Sampling Points
0 1 2 4 Km

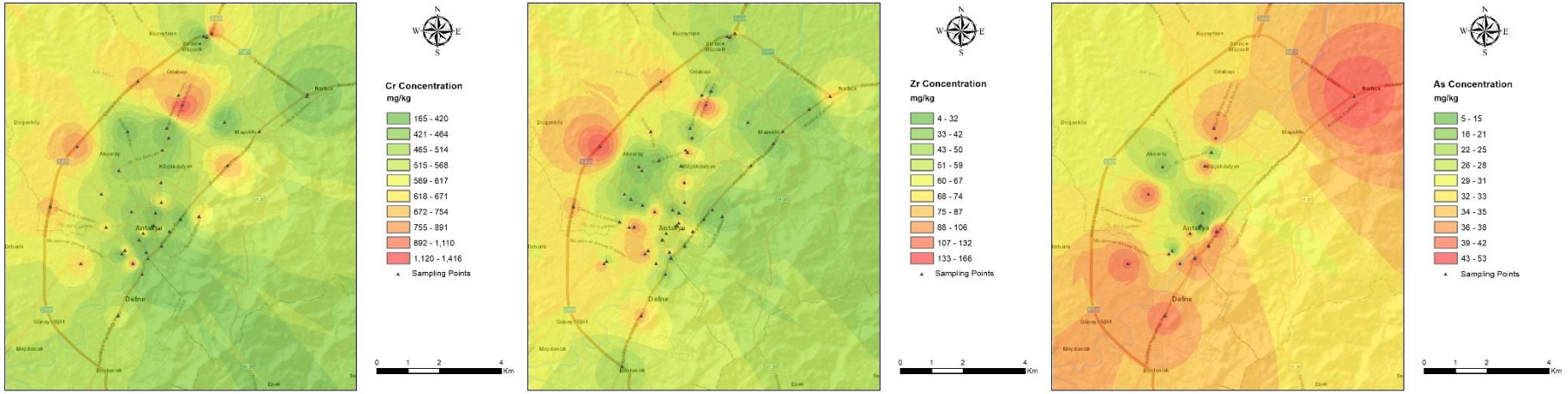

S Concentration
mg/kg
873 - 4,730
4,740 - 6,510
6,520 - 8,880
8,890 - 11,800
11,900 - 16,000
16,100 - 21,600
21,700 - 29,600
29,700 - 41,200
41,300 - 56,300
56,400 - 76,492
Sampling Points
Mn Concentration
mg/kg
460 - 953
954 - 1,110
1,120 - 1,210
1,220 - 1,310
1,320 - 1,460
1,470 - 1,610
1,620 - 1,820
1,830 - 2,150
2,160 - 2,670
2,680 - 3,523
Sampling Points
Na Concentration
mg/kg
660 - 1,350
1,360 - 1,540
1,550 - 1,670
1,680 - 1,790
1,800 - 1,920
1,930 - 2,060
2,070 - 2,280
2,290 - 2,630
2,640 - 3,160
3,170 - 3,968
Sampling Points
Antakya
Defne
0 1 2 4 Km

507

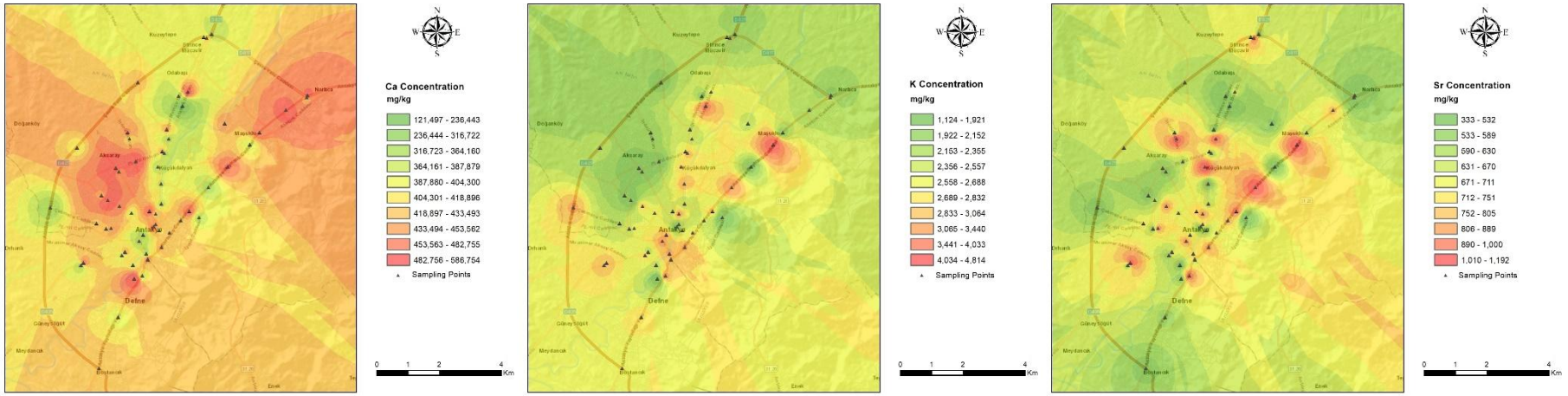

Si Concentration
mg/kg
32,860 - 74,301
74,302 - 86,141
86,142 - 93,541
93,542 - 100,200
100,210 - 107,600
107,610 - 117,220
117,230 - 132,020
132,030 - 153,480
153,490 - 182,340
182,350 - 221,560
Sampling Points
Al Concentration
mg/kg
5,689 - 10,534
10,535 - 11,955
11,956 - 12,957
12,958 - 13,959
13,960 - 14,962
14,963 - 15,714
15,715 - 16,549
16,550 - 17,886
17,887 - 20,976
20,977 - 26,991
Sampling Points
Fe Concentration
mg/kg
6,854 - 13,568
13,569 - 15,883
15,884 - 17,503
17,504 - 18,660
18,661 - 19,586
19,587 - 20,628
20,629 - 22,017
22,018 - 23,869
23,870 - 28,036
28,037 - 36,369
Sampling Points
Antakya
Defne
0 1 2 4 Km

508

509


Cr Concentration
mg/kg
165 - 420
421 - 464
465 - 514
515 - 568
569 - 617
618 - 671
672 - 754
755 - 891
892 - 1,110
1,120 - 1,416
Sampling Points
Zr Concentration
mg/kg
4 - 32
33 - 42
43 - 50
51 - 59
60 - 67
68 - 74
75 - 87
88 - 106
107 - 132
133 - 166
Sampling Points
As Concentration
mg/kg
5 - 15
16 - 21
22 - 25
26 - 28
29 - 31
32 - 33
34 - 35
36 - 38
39 - 42
43 - 53
Sampling Points
Antalya
Döşemealtı
Aksu
Kepez
Konyaaltı
Muratpaşa
Serik
Manavgat
Alanya
Gazipaşa
Finike
Kumluca
Demre
Kaş
Elmalı
Korkuteli
Gündoğmuş
Akseki
Gazipaşa
Akdeniz
Göller Bölgesi
Toros Dağları
Batı Toroslar
Orta Toroslar
Doğu Toroslar
Akdeniz Bölgesi
Km

510


Ca Concentration
mg/kg
121,497 - 236,443
236,444 - 316,722
316,723 - 364,160
364,161 - 387,879
387,880 - 404,300
404,301 - 418,896
418,897 - 433,493
433,494 - 453,562
453,563 - 482,755
482,756 - 586,754
Sampling Points
K Concentration
mg/kg
1,124 - 1,921
1,922 - 2,152
2,153 - 2,355
2,356 - 2,557
2,558 - 2,688
2,689 - 2,832
2,833 - 3,064
3,065 - 3,440
3,441 - 4,033
4,034 - 4,814
Sampling Points
Sr Concentration
mg/kg
333 - 532
533 - 589
590 - 630
631 - 670
671 - 711
712 - 751
752 - 805
806 - 889
890 - 1,000
1,010 - 1,192
Sampling Points
Antalya
Döşemealtı
Aksu
Kepez
Konyaaltı
Muratpaşa
Serik
Manavgat
Alanya
Gazipaşa
Finike
Kumluca
Demre
Kaş
Elmalı
Korkuteli
Gündoğmuş
Akseki
Gazipaşa
Akdeniz
Göller Bölgesi
Toros Dağları
Batı Toroslar
Orta Toroslar
Doğu Toroslar
Akdeniz Bölgesi
Km

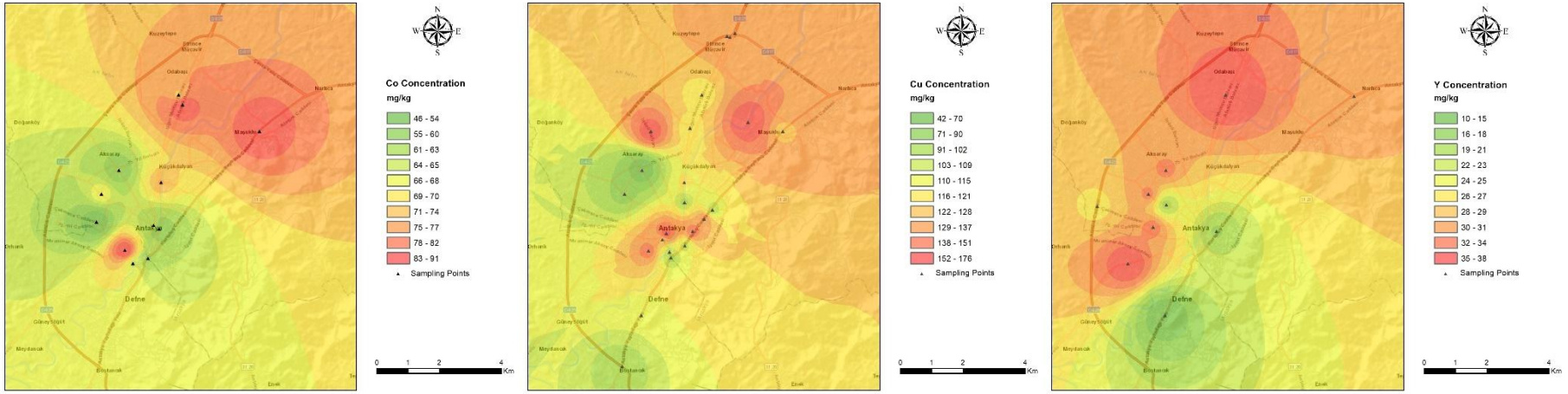
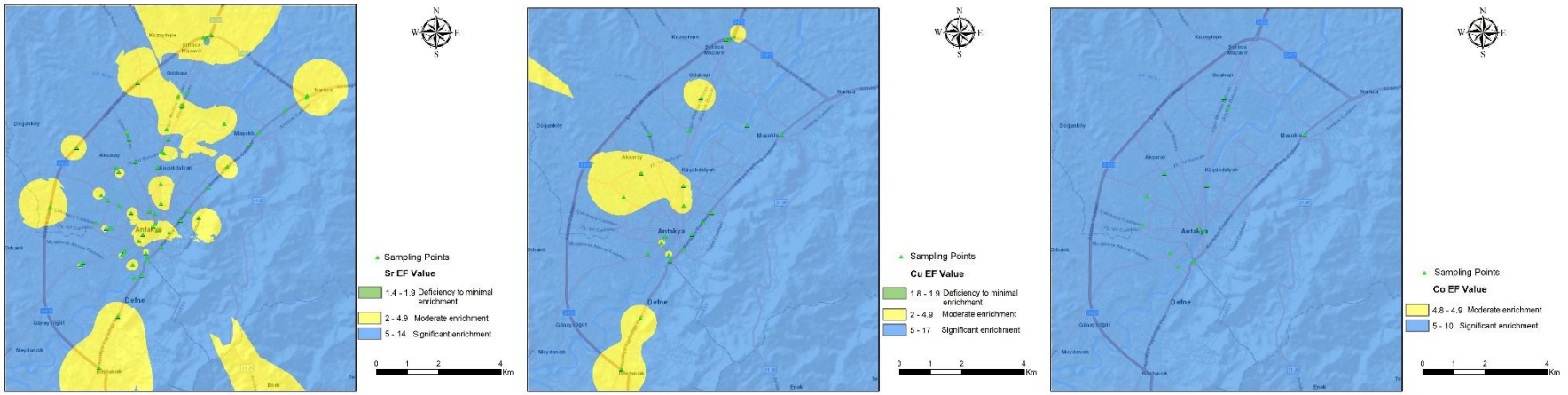
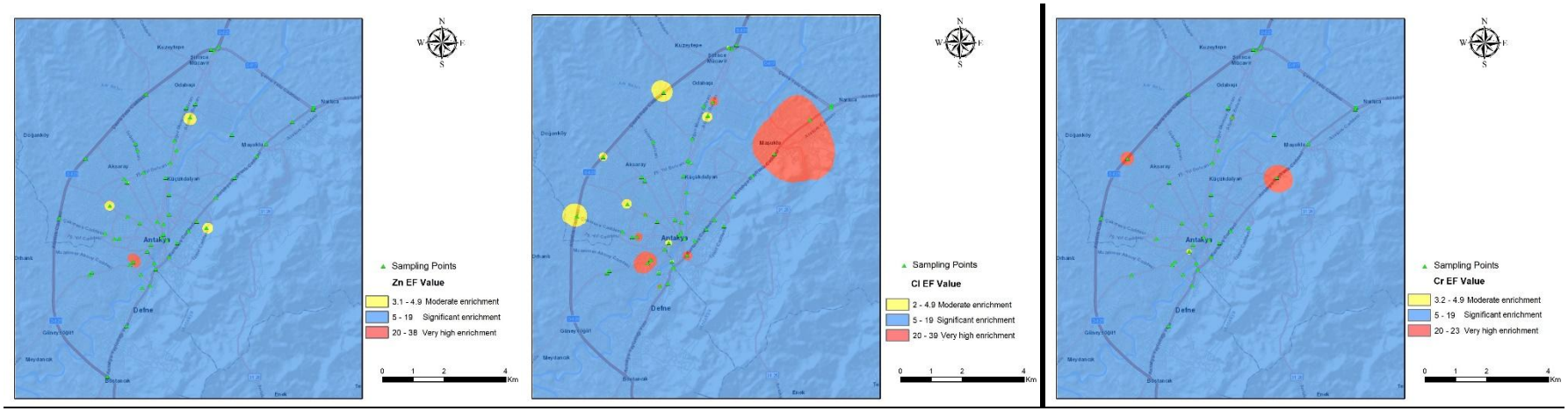


Fig. 7 Distribution maps of the analyzed elements.


Sampling Points
Sr EF Value
1.4 - 1.9 Deficiency to minimal enrichment
2 - 4.9 Moderate enrichment
5 - 14 Significant enrichment
Sampling Points
Cu EF Value
1.8 - 1.9 Deficiency to minimal enrichment
2 - 4.9 Moderate enrichment
5 - 17 Significant enrichment
Sampling Points
Co EF Value
4.8 - 4.9 Moderate enrichment
5 - 10 Significant enrichment
Antakya
Defne
Km

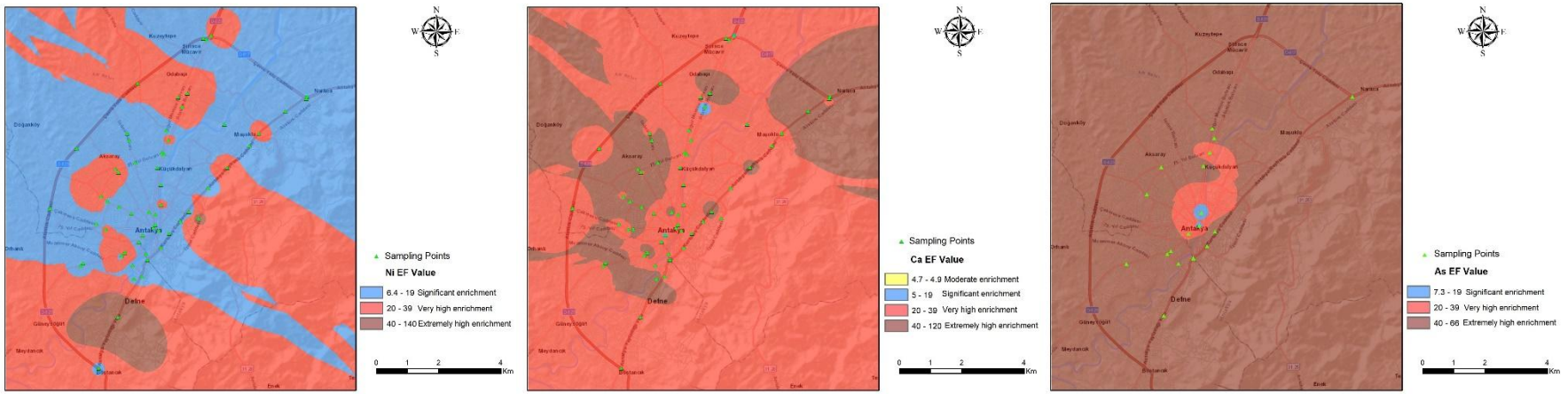
518

519

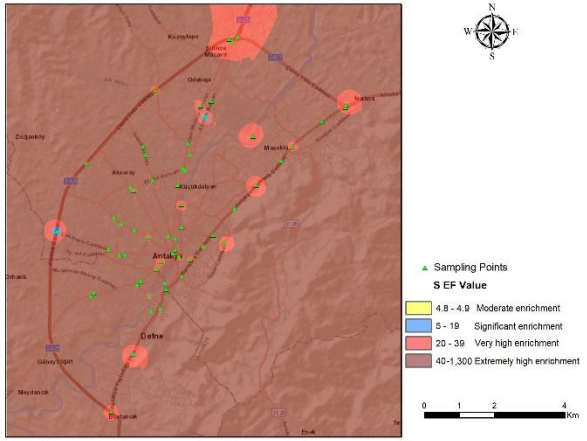

Sampling Points
Zn EF Value
3.1 - 4.9 Moderate enrichment
5 - 19 Significant enrichment
20 - 38 Very high enrichment
Sampling Points
Cl EF Value
2 - 4.9 Moderate enrichment
5 - 19 Significant enrichment
20 - 39 Very high enrichment
Sampling Points
Cr EF Value
3.2 - 4.9 Moderate enrichment
5 - 19 Significant enrichment
20 - 23 Very high enrichment
Antakya
Defne
Km

520

521



522



523 **Fig. 8** EF distribution map for the analyzed elements.

524

4. Conclusion

This study provides an integrated assessment of elemental contamination, asbestos, and other inorganic fibers in post-earthquake dust from Hatay, Türkiye. The dust was dominated by construction-related materials, while multivariate analyses indicated additional contributions from traffic, heavy machinery, industrial materials, and other urban sources. Enrichment Factor analysis showed substantial anthropogenic enrichment of several elements, and the overall Ecological Risk Index (ERI = 168.59) indicated moderate ecological risk, with As and Ni contributing the highest individual risks.

SEM-EDS analysis identified 10 confirmed asbestos fibers among 1,370 fibrous structures examined at 23 locations. These fibers were detected at six sites, mainly in areas with older informal housing, suggesting legacy asbestos-containing building materials as a likely source. Spatial analysis also revealed distinct contamination patterns associated with building age and proximity to traffic arteries.

Overall, the findings demonstrate that post-earthquake dust can contain a complex mixture of construction-derived and anthropogenic contaminants with potential environmental and public health implications. Effective dust control, proper debris management, and targeted monitoring are therefore essential. Future studies should include direct ambient-air measurements to better evaluate inhalation exposure and long-term health risks management.

Acknowledgment

Author contribution

Kadir Ulutaş involved in conceptualization, investigation, methodology, laboratory analysis, writing—original draft, review and editing, visualization, data analysis, supervision.

Enes Özkök involved in writing— review and editing, visualization.

Emre Yücer involved in visualization, data analysis, formal analysis.

Dilara Potur involved in assistance of laboratory studies.

Abdulkadir Keskin involved in writing— review and editing, statistical analysis.

Halis Simsek involved in investigation, writing— review and editing, visualization, data analysis.

Pinar Ergenekon involved in conceptualization, investigation, methodology, writing—review, visualization, data analysis.

Mehmet Salim Öncel involved in conceptualization, investigation, methodology, laboratory analysis, writing—review, visualization, data analysis.

All authors reviewed the manuscript.

Funding This study was supported by the Scientific and Technological Research Council of Türkiye (TÜBİTAK) (Project No. 123Y414).

Data availability Not applicable.

Code availability Not applicable

Declarations

Ethics approval and consent to participate All authors have read, understood, and have complied as applicable with the statement on "Ethical responsibilities of Authors" as found in the Instructions for Authors

Conflict of interest The authors declare that they have no known competing financial interests or personal relationships that could have influenced the work reported in this study.

Ethics approval Not applicable.

Consent to participate Not applicable.

Consent for publication We confirm that this manuscript has not been published elsewhere and is not under consideration by another journal. All authors have approved the manuscript and agree with this submission.

Special thanks are due to S. Aksöz, İ. Kaşık and M. Umur for their assistance in sample collection; Gebze Technical University Institute of Earth and Marine Sciences and Istanbul Medeniyet University Science and Advanced Technology Application and Research Center for their assistance with the analysis processes.

References

AA (2023) Depremlerin vurduğu Hatay'da en ağır yıkım Antakya'da. Last accessed: 25 May 2025. https://www.aa.com.tr/tr/asrin-felaketi/depremlerin-vurdugu-hatayda-en-agir-yikim-antakyada/2866977.

Abujayyab SK, Öztürk A, Canbulat O, Yücer E, Abu Amr SS (2025) Impact of the 2023 earthquake in Türkiye on air quality using Sentinel-5P satellite data: a comparative analysis. Environmental Earth Sciences, 84(19), 537.

AÇISGUR, (2019) T.C. Aile, Çalışma ve Sosyal Hizmetler Bakanlığı İş Sağlığı ve Güvenliği Genel Müdürlüğü, Asbestle Çalışmalarda İş Sağlığı ve Güvenliği Uygulama Rehberi (AÇISGUR). Ankara, Türkiye. https://www.csgb.gov.tr/Media/cowaxrcv/asbestle-calismalarda-is-sagligi-ve-guvenligi-uygulama-rehberi_05082019.pdf

Akhter MS, Madany IM (1993) Heavy metals in street and house dust in Bahrain. Water. Air. and Soil Pollution. 66(1–2). 111–119. https://doi.org/10.1007/BF00477063

Azarmi F, Kumar P (2016) Ambient exposure to coarse and fine particle emissions from building demolition. Atmospheric environment, 137, 62-79. https://doi.org/10.1016/j.atmosenv.2016.04.029

Bencko V, Rameš J, Fabiánová E, Pešek J, Jakubis M (2009) Ecological and human health risk aspects of burning arsenic-rich coal. Environmental geochemistry and health, 31(Suppl 1), 239-243.

Briffa J, Sinagra E, Blundell R (2020) Heavy metal pollution in the environment and their toxicological effects on humans. Heliyon, 6(9), e04691. https://doi.org/10.1016/j.heliyon.2020.e04691

ÇBS (2023) Bakan kurum: 582 bin bağımsız bölüm ve 202 bin binanın acil yıkılacak, ağır hasarlı veya yıkık olduğu tespitini yaptık. Last accessed: 25 May 2023. https://www.csb.gov.tr/bakan-kurum-582-bin-bagimsiz-bolum-ve-202-bin-binanin-acil-yikilacak-agir-hasarli-veya-yikik-oldugu-tespitini-yaptik-bakanlik-faaliyetleri-38458

Cesari D, Contini D, Genga A, Siciliano M, Elefante C, Baglivi F, Daniele L (2012) Analysis of raw soils and their re-suspended PM10 fractions: characterisation of source profiles and enrichment factors. Applied Geochemistry, 27(6), 1238-1246.

Delibašić Š, Đokić-Kahvedžić N, Karić M, Keskin I, Velispahić A, Huremović J, Herceg K, Selimović A, Silajdžić S, Žero S, Gojak-Salimović S, Partić A,.Pašalić A (2020) Health risk assessment of heavy metal contamination in street dust of federation of Bosnia and Herzegovina. Human and Ecological Risk Assessment: An International Journal. 27(5), 1296-1308. https://doi.org/10.1080/10807039.2020.1826290

DHA (2023) Deprem atıklarının yönetiminde zamanla yarış. Last accessed: 25 May 2025. https://www.dha.com.tr/yerel-haberler/izmir/deprem-atiklarinin-yonetiminde-zamanla-yaris-2215258

Dimiskovska B (2010) Environmental risks due to debris containing asbestos in post-earthquake conditions. Acta Geodaetica et Geophysica Hungarica, 45(3), 299-306. https://doi.org/10.1556/AGeod.45.2010.3.4

Ding Z, Wang Y, Zou PX (2016) An agent based environmental impact assessment of building demolition waste management: Conventional versus green management. Journal of Cleaner Production, 133, 1136-1153. https://doi.org/10.1016/j.jclepro.2016.06.054

Ersöz F, Ersöz T (2022) İstatistik-1. Seçkin Kitabevi. Ankara, Türkiye.

Fuge R (2012). Anthropogenic sources. In Essentials of medical geology: Revised Edition (pp. 59-74). Dordrecht: Springer Netherlands.

González MF, Saadatkhah N, Patience GS (2024) Experimental methods in chemical engineering: X-ray fluorescence—XRF. The Canadian Journal of Chemical Engineering, 102(6), 2004-2018.

Güney NN, Yılmaz B (2023) Deprem Sonrası Çevre Kirliliğini Önlemek: Geçici Depolama Alanları, Kahramanmaraş Merkezli Depremler Sonrası İçin Akademik Öneriler. Editörler: Öztürk, M., Kırca, M. Özgür Yayınları.

Guo M, Wei L, Yan H, Duan Z, Niu Z, … Xiao C (2021) Exposure to ambient air pollution during trimesters of pregnancy and childhood allergic diseases in Wuhan. China. International Journal of Environmental Health Research. 1-11. https://doi.org/10.1080/09603123.2021.1929873

Hakanson L (1980) An ecological risk index for aquatic pollution control. A sedimentological approach. Water research, 14(8):975-1001. https://doi.org/10.1016/0043-1354(80)90143-8

IARC International Agency for Research on Cancer (2012) Arsenic, metals, fibres, and dusts. Volume 100 C. A review of human carcinogens. IARC Monographs on the Evaluation of Carcinogenic Risks to Humans. Lyon (FR): International Agency for Research on Cancer, ASBESTOS, 219-315.

Ite AE, Udousoro II, Ibok. UJ (2014) Distribution of some atmospheric heavy metals in lichen and moss samples collected from Eket and Ibeno Local Government Areas of Akwa Ibom State. Nigeria. American Journal of Environmental protection. 2(1). 22–31. https://doi.org/10.12691/env-2-1-5

Jacobs DE, Cali S, Welch A, Catalin B, Dixon SL, Evens A, Bartlett J (2013) Lead and other heavy metals in dust fall from single-family housing demolition. Public health reports, 128(6), 454-462. https://doi.org/10.1177/003335491312800605

Kafle HK, Khadgi J, Ojha RB, Santoso M (2022) Concentration, Sources, and Associated Risks of Trace Elements in the Surface Soil of Kathmandu Valley, Nepal. Water, Air, and Soil Pollution, 233(2). https://doi.org/10.1007/s11270-021-05444-1

Kanwar VS, Sharma A, Srivastav AL, Rani L (2020) Phytoremediation of toxic metals present in soil and water environment: a critical review. Environmental Science and Pollution Research, 27, 44835-44860. https://doi.org/10.1007/s11356-020-10713-3

Kara M (2020) Assessment of sources and pollution state of trace and toxic elements in street dust in a metropolitan city. Environmental Geochemistry and Health. 42(10). 3213–3229. https://doi.org/10.1007/s10653-020-00560-z

Kravkaz Kuşçu İS, Kılıç Bayraktar M, Tunçer B (2022) Determination of Heavy Metal (Cr, Co, and Ni) Accumulation in Selected Vegetables Depending on Traffic Density. Water, Air, Soil Pollution, 233(6), 224. https://doi.org/10.1007/s11270-022-05697-4

Kumari S, Jain MK, Elumalai SP (2021). Assessment of pollution and health risks of heavy metals in particulate matter and road dust along the road network of Dhanbad, India. Journal of health & pollution, 11(29), 210305.https://doi.org/10.5696/2156-9614-11.29.210305

Lancia A, Musmarra D, Prisciandaro M (2000) Calcium sulfate. Kirk-Othmer Encyclopedia of Chemical Technology, 1-22.

Li HC, Chiueh PT, Liu SP, Huang YY (2017) Assessment of different route choice on commuters' exposure to air pollution in Taipei. Taiwan. Envıronmental Scıence and Pollutıon Research. 24(3). 3163-3171. https://doi.org/0.1007/s11356-016-8000-7

Liu E, Yan T, Birch G, Zhu Y (2014) Pollution and health risk of potentially toxic metals in urban road dust in Nanjing, a mega-city of China. Science of the Total Environment, 476, 522-531. https://doi.org/10.1016/j.scitotenv.2014.01.055

Long X, Shao C, Wang H, Wang J (2016) Single-source-precursor synthesis of SiBNC-Zr ceramic nanocomposites fibers. Ceramics International, 42(16), 19206-19211.

Long X, Shao C, Wang H, Wang J (2016) Single-source-precursor synthesis of SiBNC-Zr ceramic nanocomposites fibers. Ceramics International, 42(16), 19206-19211.

Maden S (2023) 6 Şubat 2023'te Kahramanmaraş'ta Yaşanan Depremler Ekseninde Türkiye'de Deprem Haberciliğine Bakış: Prof. Dr. Süleyman İrvan ile Söyleşi. Etkileşim, (11), 406-420.

Manasreh WA (2010) Assessment of trace metals in street dust of Mutah city. Karak. Jordan. Carpathian Journal of Earth and Environmental Sciences. 5(1). 5–12. WOS:000276785500001

Marjovvi A, Soleimani M, Mirghaffari N, Karimzadeh H, Yuan Y, Fang L (2022) Monitoring, Source Identification and Environmental Risk of Potentially Toxic Elements of Dust in Isfahan Province, Central Iran. Bulletin of Environmental Contamination and Toxicology, 1-8. https://doi.org/10.1007/s00128-021-03446-7

Mason B (1966) Principles of geochemistry, 3rd edn. John Wiley, New York, NY, USA.

Metin A, Kişi M, Kalender S (2023) Deprem Bölgelerinde Deprem Sonrası Oluşabilecek Halk Sağlığı Riskleri ve Çözüm Önerileri. Kahramanmaraş Merkezli Depremler Sonrası İçin Akademik Öneriler. Editörler: Öztürk, M., Kırca, M. Özgür Yayınları.

Moskovchenko D, Pozhitkov R, Soromotin A, Tyurin V (2022) The content and sources of potentially toxic elements in the road dust of surgut (Russia). Atmosphere, 13(1), 30. https://doi.org/10.3390/atmos13010030

Nagalakshmi R, Prasanna K, Chandar SP (2016) Water quality analysis using gis interpolation method in serthalaikadu Lagoon. east coast of India. Rasayan Journal of Chemistry. 9(4). 634-640. https://rasayanjournal.co.in/admin/php/upload/73_pdf.pdf

Nedobukh TA, Semenishchev VS (2019) Strontium: source, occurrence, properties, and detection. In Strontium Contamination in the Environment (pp. 1-23). Cham: Springer International Publishing.

Oral T, Ensari Özay M, Uçan R, Aker D, Can E, Altınten B (2025) Measurement and Evaluation of Dust Concentrations in the Air After the Kahramanmaraş Earthquake in Turkey. International Journal of Environmental Research and Public Health, 22(4), 649. https://doi.org/10.3390/ijerph22040649

Sadeghdoust F, Ghanavati N, Nazarpour A, Babaenejad T, Watts MJ (2020) Hazard. ecological. and human health risk assessment of heavy metals in street dust in Dezful. Iran. Arabian Journal of Geosciences. 13(17). 1–14. https://doi.org/10.1007/s12517-020-05915-5

Shafie S, Mohamad S, Rameli N, Pasaribu S (2021) Analysis of Urban Air Pollution and The Effectiveness of Air Pollution Control Policy in Malaysia: Case Study in Klang Valley. Malaysia. Jurnal Cıta Hukum-Indonesıan Law Journal. 9(1). 13-28. https://doi.org/10.15408/jch.v9i1.20018

Smoliński A, Stempin M, Howaniec N (2022) Application and validation of analytical software (SQX) for semi-quantitative determination of the Main chemical composition of solid, bulk and powder fuel samples by wavelength dispersive X-ray fluorescence technique. Energies, 15(19), 7311.

Stevulova N, Estokova A, Holub M, Singovszka E, Csach K (2020) Characterization of demolition construction waste containing asbestos. and the release of fibrous dust particles. Applied Sciences. 10(11). 4048. https://doi.org/10.3390/app10114048

Tasdemir Y, Kural C, Cindoruk SS, Vardar N (2006) Assessment of trace element concentrations and their estimated dry deposition fluxes in an urban atmosphere. Atmospheric Research. 81(1). 17–35. https://doi.org/10.1016/j.atmosres.2005.10.003

Tokkamiş N, Uraz C (2022) Investigation of Asbestos Hazard in Urban Transformation Areas in Karşiyaka in İzmir Province. International Refereed Journal of Engineering and Sciences, 39.

696 Ulutaş K (2022) Risk assessment and spatial distribution of heavy metal in street dusts in the densely industrialized
697 area. Environmental Monitoring and Assessment, 194(2), 99. https://doi.org/10.1007/s10661-022-09762-
698 7

699 Ulutaş K (2023a) Assessment of the pollution level, microscopic structure, and health risk of heavy metals in
700 surface dusts in a sports field. Pamukkale University Journal of Engineering Sciences, 29(5), 529-536.
701 https://doi.org/10.5505/pajes.2022.50880

702 Ulutaş K (2023b) Spatial distribution, contamination levels, source identification and human health risk
703 assessment of potentially toxic elements in street dust in urban area in Libya. Soil and Sediment
704 Contamination: An International Journal, 32(1), 125-146.
705 https://doi.org/10.1080/15320383.2022.2136139

706 Ulutaş K, Jasim OAF, Sevinç HK, Karaş İR, Öztürk F (2025) Pollution characteristics and health risk assessment
707 of potentially toxic elements of street dust in the ancient civilization city of Baghdad, Iraq. Environmental
708 Geochemistry and Health, 47(9), 373.

709 Wang XJ, Liu RM (2005) Spatial analysis and eutrophication assessment for chlorophyll a in Taihu Lake.
710 Environmental Monitoring and Assessment. 101. 167-174. https://doi.org/10.1007/s10661-005-9154-9

711 Wieland E, Tits J, Kunz D, Dähn R (2008) Strontium uptake by cementitious materials. Environmental science &
712 technology, 42(2), 403-409.

713 Witek J, Kusiorowski R (2017) Neutralization of cement-asbestos waste by melting in an arc-resistance
714 furnace. Waste Management. 69. 336-345. https://doi.org/10.1016/j.wasman.2017.08.017

715 Xie Y, He W, Zhang X, Cui J, Tian X, Chen J, Guo Y (2021) Association of air pollution and greenness with
716 carotid plaque: A prospective cohort study in China. Environmental Pollution. 273. 1-7.
717 https://doi.org/10.1016/j.envpol.2021.116514

718 Xu H, Ho SSH, Cao J, Guinot B, Kan H, Shen Z, ... Huang R (2017) A 10-year observation of PM2. 5-bound
719 nickel in Xi'an, China: Effects of source control on its trend and associated health risks. Scientific
720 reports, 7(1), 41132.associated health risks. Scientific reports, 7(1):1-10.
721 https://doi.org/10.1038/srep41132

722 Yang K, Yoo KC, Jung J (2020) Quantitative analysis of asbestos-containing materials using various test
723 methods. Minerals, 10(6), 568. https://doi.org/10.3390/min10060568

724